Lagrangian Modeling of Industrial Point-source Plumes in the Houston-Galveston Area

FINAL REPORT
TCEQ Contract No. 582-2-48649-01

Submitted by

Noor V. Gillani, PI
Yuling Wu, Co-I

Earth System Science Center
University of Alabama in Huntsville
Huntsville, AL 35899

March 2003

TABLE OF CONTENTS

ABSTRACT

A previous preliminary diagnostic lagrangian modeling study using the NCAR Electra aircraft data of the TexasAQS 2000 field study had suggested that emissions of certain reactive alkenes from industrial point sources (IPSs) in the Houston-Galveston (H-G) area may be grossly under-estimated in the existing emissions inventory (EI), that the VOC and NOx co-emissions from such sources may be of comparable magnitude and the cause of the observed rapid ozone production in compact areas or transient high ozone events (THOEs). That study presented modeling results only for the relatively isolated plumes from the Sweeny and Freeport source complexes. This work was undertaken to perform a much more rigorous diagnostic lagrangian modeling study using the same dataset, and aimed also at the more densely packed IPSs in the Ship Channel Complex (SCC). The main objectives were (1) to obtain more accurate estimates of the NOx and VOC emissions from all the major IPSs in the H-G area, including the sources in the SCC, and (2) to test the ability of lagrangian plume modeling to capture the observed fine structure of the THOEs. To perform this study, the state-of-the-art UAH-LRPM (University of Alabama in Huntsville --- Lagrangian Reactive Plume Model) was upgraded from a single-plume model to a multi-interacting-plumes model. The diagnostic study was also focussed on a particular case study, that of the NCAR Electra sampling mission of 28 August 2000, which was ideal for the purpose, given the corresponding relatively simple meteorology (persistent S-SE on-shore winds in the study area) and relatively subdued chemistry (maximum ground-level observed ozone of 112 ppb downwind of the SCC).

The H-G area has five major complexes of IPSs, viz. the relatively isolated ones at Sweeny, Freeport and Chocolate Bayou in the south part of the study area, and Texas City and SCC further to the north and east, where the plumes from the many sources commonly become mixed into an intense megaplume. The many sources from these complexes were aggregated into 35 composited sources to be individually simulated (1 from Sweeny, 3 from Freeport, 2 from Bayou, and 29 from Texas City-SCC) in the multi-interacting-plumes model. Starting with the emission rates of NOx and VOC species as in the EI, simulations were performed iteratively with increasing emission rates of these species until good match was obtained between observed and simulated downwind species concentrations. All simulations were based on the CB4 chemical mechanism, in which ethene is modeled explicitly (as ETH) and the other alkenes (olefins) are grouped into a single class called OLE. For each source complex, separate simulations were made for each sampling of the plume at a downwind distance by the aircraft. Special care was taken to make the simulated plume dynamics as close to observed as possible, using both the aircraft data and the rich available meteorological database.

We found a more or less consistent story of the inferred emission picture for all five source complexes: typically, the inferred NOx emissions were within a factor of two (always greater) of the EI values, with the exceptions that the Bayou sources and some of the sources in the western half of the SCC had inferred NOx emission rates which were 3-5 times greater than their EI values; except for the few power plants, the inferred ETH and OLE emission rates from most of the IPSs were 1 to 2 orders of magnitude greater than their EI values, such that they were generally comparable to the co-emitted NOx emission rates. Such co-emissions of NOx and reactive VOC resulted in very rapid chemistry producing ozone and other secondary formations (e.g., NOz and aldehydes). The multiplume LRPM performed remarkably well for this relatively simple meteorological scenario in capturing details of the complex interacting plumes even from the SCC, for the primary emission species as well as for the secondary species. The report

provides a fairly detailed description of the diagnostic simulations and results, and also a fairly detailed conclusions and recommendations section.

1. INTRODUCTION

A major intensive 3-D field measurement program was conducted in the Houston-Galveston area of Texas in the Summer of 2000 (the Texas 2000 Air Quality Study, or TexAQS). An important preliminary finding of an accelerated science evaluation of ozone formation in the area, based on comparison of field observations (aircraft and ground-based) and simplified diagnostic Lagrangian reactive plume modeling (LRPM) using the latest available point-source emissions inventory (EI), was that emissions estimates of certain reactive VOCs from large industrial point-sources may be grossly under-estimated in the EI (TNRCC, 2002). In particular, the new finding suggested that emissions of the low molecular weight reactive alkenes, especially ethene and propene, from such sources, which are particularly concentrated in the Ship Channel area to the northwest of Galveston Bay, may be 1 to 2 orders of magnitude higher than in the EI, and comparable to the co-emissions of NO_x, and that these emissions, together, may be largely responsible for the observed very rapid and efficient formation of ozone in the corresponding plumes (Trainer, 2001). This finding, if true, has serious implications for the new SIP which is under development, particularly in terms of development of an optimum ozone control strategy based on *combined* VOC and NO_x control. It would also explain why air quality grid models based on the EI have failed to simulate the observed rapid and high ozone events in H-G. An urgent need existed to test this important finding more rigorously, based on a top-down (observation-based) approach of emissions verification, using the state-of-the-art ambient measurements of TexAQS. This report presents findings of such a rigorous diagnostic modeling study targeted at the various clusters of industrial point sources in the Houston-Galveston area. It is based on use of the TexAQS data and a state-of-the-art LRPM (the UAH-LRPM), which was specifically enhanced for this project to facilitate modeling of multiple interacting plumes such as in the ship channel complex. The primary purpose of this project was to answer the following specific questions:

1. Can this type of LRPM reproduce compact areas of high ozone such as those observed during specific episode days by TexAQS 2000 researchers and by TNRCC's network of monitoring sites?
2. Can this type of LRPM reproduce the rates of ozone formation and ozone yields observed in specific plumes during specific episode days during TexAQS 2000?
3. What emission rates of ozone precursors can be inferred from coupling the observations with the upgraded multi-plume UAH-LRPM?

As much as possible, such verification was to be targetted at individual large point sources or source complexes. In the case of most cities, the largest emissions uncertainties are generally associated with reactive VOC emissions from *area and mobile* sources. The H-G area, however, is different from most other cities in that a relatively limited number of large industrial *point-*sources contribute an unusually large component of the reactive VOC emissions here, and their emission inventories are now suspect, hence the focus on such sources.

2. RELEVANT PRIOR FINDINGS OF TexAQS --- BACKGROUND

The Houston-Galveston (H-G) and the Dallas-Ft. Worth (DFW) areas have about the same population (~ 4 million), as well as area-source and mobile-source emissions (based on current EIs) of both the ozone precursors, VOC and NO_x. Yet, H-G has far more annual exceedances of the 1-h ozone NAAQS (129 v 28), a much higher ozone design value (199 ppb v 131 ppb), and a

significantly longer ozone season, peaking in late August/early September (Breitenbach, 2002). The main reason appears to be that H-G has much higher emissions (an order of magnitude, or more) of both VOC and NO_x from major *point* sources, particularly, industrial point sources which co-emit both VOC and NO_x in large quantities. There is a particularly dense concentration of such sources in the Ship Channel complex (SCC) of petrochemical industry to the northwest of Galveston Bay and east of the Houston urban core (see Fig. 1). The highest monitored ozone concentrations occur most frequently close to the SCC, east of the urban core (TNRCC, 2001a). Co-emissions of large quantities of reactive VOC and NO_x from such industrial point sources may react very quickly, resulting in very rapid and efficient ozone production, much more so than in plumes of typical urban core emissions (Houston and most other cities) and of large power plant emissions (Trainer, 2001; Ryerson et al., 2001). Such industrial source plumes of high ozone are also rather compact and dynamic, with the ozone peak advecting sequentially over particular downwind surface monitoring sites, registering distinct transient high ozone events (*THOEs*) at the impacted sites (TNRCC, 2001a). The ozone rise rates of these *THOEs*, and related ozone production rates, frequently exceed 40 ppb/h, and as much as 200 ppb/h, as measured at surface sites and in aircraft (TNRCC, 2001a; Daum, 2002). These are much higher than those observed in most other cities. Lidar measurements of vertical profiles of ozone and aerosol backscatter reveal complex cross-sectional structure in such plumes (Senff et al., 2001).

Another important reason for the distinct spatial-temporal distribution of ozone in H-G appears to be that meteorology related to the fairly frequent land/sea breeze recirculations, occuring on about 37% of the days in August-September (Breitenbach, 2002), is also more conducive to high ozone formation and buildup (TNRCC, 2001b). On such days, a conceptually distinct local flow pattern prevails: light nocturnal flow, turning from W at midnight to NW by 6 a.m., promotes accumulation of urban precursor emissions in a shallow mixing layer, and their slow drift toward Galveston Bay; by noon, the winds have rotated to the E, and then strengthen from the SE as the sea breeze comes in during the afternoon; in the meanwhile, under the daytime sunlight and heat, these precursors convert to ozone and related smog, being reinforced by the rapidly reacting embedded emissions from the elevated industrial point sources into the rising morning mixing layer and the deep afternoon mixing layer. The resulting soup in the afternoon consists of a fairly broad area of high ozone, with embedded, relatively compact, peaks of rapidly-formed ozone in industrial source plumes.

The existence of the moving *THOEs* downwind of the industrial source complexes was suspected even before TexAQS, but there was much speculation about the mechanism(s) of the rapid chemistry causing them. The following possible chemical mechanisms had been hypothesized as the likely cause(s) (TNRCC, 2001a): (a) high co-emissions of reactive VOCs and NOx from industrial sources, including possible upset emissions; (b) chemical pathways for ozone formation other than those in current photochemical models, such as atomic chlorine reactions in the presence of alkanes (based on detection of products of such chemistry), and possible heterogeneous reactions on aerosol surfaces; and (c) enhanced (observed) nocturnal radical production and accumulation from ozone-alkene or other pathways, possibly contributing to accelerated daytime ozone production. Aircraft observations and diagnostic reactive plume modeling under TexAQS (Trainer, 2001; Ryerson et al., 2001) appear to suggest strongly that item (a) above may be the most likely and dominant cause, even under conditions of routine (rather than upset) emissions. Emissions of NOx from the industrial plumes appear to be

consistent with the latest TNRCC emission inventories (EIs), but emissions of low-molecular-weight reactive alkenes (particularly ethene, propene and 1,3-butadiene) appear to be MUCH higher than in the EIs (up to two orders of magnitude for ethene and at least one order of magnitude for propene), making these VOC emissions comparable with (or even higher than) the corresponding NO_x emissions. Such high co-emissions of these reactive VOCs and NOx can give the observed rapid and efficient production of not only ozone, but also of correlated secondary species such as aldehydes and PANs, based on standard chemical mechanisms currently used in photochemical models (e.g., CB-IV and SAPRC). It may, therefore, not be necessary to invoke substantial participation of the other hypothesized mechanisms (e.g., chlorine-alkane, heterogeneous chemistry, or nocturnal radical production). The limited role of chlorine chemistry has also been confirmed by Tanaka et al (2000; 2001), using chlorine-related data of Riemer et al (2001) and photochemical modeling including appropriate chlorine chemistry. Aircraft observations of only small quantities of products of isoprene chemistry (e.g., MPAN) also indicate a relatively minor role of isoprene in the rapid and efficient formation of ozone in the industrial plumes, especially during southerly flow. Lack of significant correlation between observed ozone and Beryllium-7 (a tracer of stratospheric origin) at the LaPorte surface monitoring site also ruled out significant contribution of stratospheric ozone to the *THOEs* (Wood, 2002).

The above speculations about the chemistry contributing to rapid and efficient ozone production close to the industrial point sources left out one other *potential* important mechanism, that related to possible enhancement of reaction rates (of the VOC-NOx chemistry) due to highly-correlated turbulent fluctuations in the concentrations of co-emitted species (VOC, NOx), or directly related other reactants, particularly oxidants (ozone, odd-H radicals). Such enhancement is not currrently included in the grid models used for SIP calculations or the LRPMs used in diagnostic studies. To include such effects, model simulations must explicitly resolve large turbulent eddies (Large Eddy Simulations, LES, with detailed chemistry), or include parameterizations of the turbulent chemistry, particularly in industrial plume modeling close to the source. A preliminary application of LES-with-chem to an isolated point source plume with large NOx and ethene co-emission has shown significant enhancement of the chemistry by turbulent effects (Herwehe et al., 2002). If so, the high inferred estimates of ethene and propene emissions from the industrial sources in the preliminary findings of the accelerated science evaluation could themselves be in significant error, and may be considered to be upper-bound estimates.

In the present project, the focus was on mechanism (a), i.e., high co-emissions of reactive VOCs and NOx from industrial sources, and the approach used in the study is that of diagnostic LRPM and TexAQS data. In a separate project funded by the Houston Advanced Research Center (HARC), the significance of turbulent fluctuating chemistry in such point-source plumes is being explored.

3. SELECTION OF THE CASE STUDY --- 28 August 2000

We wished to perform top-down emissions verification (TD_EV) of ozone precursor emissions (VOC and NOx) by diagnostic Lagrangian modeling using 3-D field observations, principally those made during the NCAR Electra aircraft (operated by NOAA's Aeronomy lab) traverses in the plumes of the target industrial point sources (IPSs, particularly those concentrated in the five clusters identified as Sweeny, Freeport, Chocolate Bayou, Texas City and Ship Channel

Complex --- see Fig. 1) for a selected case study day, for which ambient meteorological and chemical conditions were most favorable for our purpose. Such a Lagrangian study of TD_EV is most suitable under relatively uniform and steady meteorological conditions, as when the winds are sustained in the same direction for a few hours, fairly steady in time and uniform in space. The main requirement is that the quantity and identity of the emission mass remain as close to the emission condition as possible (except for dispersion), and that it be measured as fully as possible. Thus, downwind measurements of the target precursors closest to the target source(s) are the most desirable (minimal chemistry and removal, and mixing with extraneous matter). However, the aircraft VOC data are sparse point measurements only, and rather inadequate for such purpose. We must, therefore, also exploit other continuous and semi-continuous data which are sensitive to the VOC emissions. Such data include ozone and PAN (continuous), and HCHO (semi-continuous). These variables, however, represent secondary species formed from the plume VOC-NOx chemistry, and their concentrations become most pronounced at intermediate distances from the sources. Diagnostic modeling can provide source-oriented 3-D estimates of both the precursors (for near-source analysis) and the measured secondary species (for intermediate-range analyses).

We selected August 28, 2000 as a near-ideal case study for our analyses. On that day, the winds were consistently from S-to-SE, with the NCAR Electra making crosswind (E-W) traverses across the H-G area at nine sections, four upwind (south) of the ship channel, and five downwind (north) of it (the closest-in of these being about 10 km downwind). Figure 2 presents the Electra flight map of 28 August, with measured ozone distribution along the flight trajectory. It shows the more "isolated" plumes from Sweeny, Freeport A/B, Chocolate Bayou and Texas City being sampled in the southernmost traverses, and the SCC merged plume in the five northernmost traverses, these latter at downwind distances (from the SCC) ranging from 10 to 100 km. Apart from the relatively simple/steady/uniform meteorology of this day, this was also a day with limited chemistry (also desirable in a study with particular focus on the primary emissions), with the highest surface level concentration of ozone measured in the area (north of the SCC) on this day being only 112 ppb. The data base for the diagnostic study is also rich for this day, including the excellent coverage of the Electra, considerable amount of surface chemical sampling and upper air meteorological soundings, plus, availability of Eulerian sub-regional simulations of gridded emissions, meteorology and chemistry at fairly fine spatial-temporal resolution, to provide some of the input information needed to drive the Lagrangian modeling.

4. UAH-LRPM: Single-plume Version and Multi-plume Upgrade

4.1 Single-plume Version

The model applied here is the current version of the UAH-LRPM (University of Alabama in Huntsville --- Lagrangian Reactive Plume Model). It originated as the Gillani-LRPM (Gillani 1986), and further evolved as UAH-LRPM following its upgrade for use as the building block of the Plume-in-Grid (PinG) module (Gillani et al., 1998; Gillani and Godowitch, 1999) of EPA's urban-regional modeling system, Models-3/CMAQ (EPA 1999). Conceptually, the model simulates the time-dependent, two-dimensional concentration evolution within a semi-infinite lagrangian vertical slab moving with the average transport wind, which may vary with time (in speed and direction) along the slab trajectory. It does not allow for wind shear effects; hence, its application is best suited in the convective summer boundary layer during the daytime, and

particularly when wind shear effects are not very significant. Such was indeed the condition in its application to the simulations of the case study presented here (28 August 2000). The slab framework of our LRPM permits arbitrary spatial resolution (externally specified) in both the crosswind (y) and the vertical (z) directions. The model is designed to simulate the change in concentration of all modeled chemical species in each slab cell, in response to emissions, their subsequent lateral and vertical dilution and diffusion, gas-phase chemistry, dry deposition at the surface (for selected species), and an optional linear volumetric removal process (proportional to the local species concentration), which may be applied for selected species, if deemed necessary. The model is quite suitable for plume(s) with inhomogeneous (including asymmetric) spatial concentration distributions in the plume(s). Emissions may be from an elevated point source at a given time, as well as continuously from the surface in a spatially-temporally variable gridded areal distribution. The chemistry can be based on any externally specified chemical mechanism; the CB-IV mechanism, with the condensed Carter isoprene scheme (Carter, 1996), is used in all simulation results presented here.

Horizontal diffusion is based on horizontally homogeneous eddy diffusion (K_y), but different options are available for vertical diffusion, including height-dependent eddy diffusion (K_z), asymmetric convective mixing (ACM, Pleim and Chang 1992) in the convective boundary layer (CBL), and a combination of eddy diffusion (in the lowest 15% of the CBL) and ACM (higher up in the CBL). This last combination best simulates the observed profiles of species emitted at the surface, which have significant gradients in the lowest part of the CBL, but a more well-mixed profile higher up. This hybrid option is exercised in all simulations included in this report. The vertical domain of the model must extend to at least the peak mixing height of the day, in order to allow for realistic fumigation or entrainment of mass from above the mixing layer into the mixing layer as this layer grows during the morning hours. A constant small value of K_z is used for vertical diffusion in the aloft layers outside the CBL.

Every model run of a point source plume actually involves two parallel slab simulations, one with the point-source emission into a dynamic and kinetic background (the "plume" run), and another without such emission (the "background" run). Both runs include crosswind and vertical spatial resolution, the same distribution of surface emissions, and the same physical-chemical processes. From the difference between the two parallel simulations, we can determine plume excess concentrations above the background in a very local sense. The spatial resolution of the background is fixed in time: the background slab has a constant crosswind width (chosen to be significantly wider than the widest simulated plume width) and a constant horizontal spatial resolution (typically, 1.5 km); the vertical domain is chosen to significantly exceed the peak mixing height during the full simulation period, and is resolved into 32 layers of varying thicknesses, the lowest five typically chosen to be 10m thick each, and the coarsest ones above the mixing layer to be 100 m. The spatial resolution of the plume slab is variable in time. Horizontally, the expanding plume width, $W_p(t)$, can be divided into an arbitrary number of plume pillars of arbitrary widths. Our common practice in the simulation of isolated single plumes is to divide $W_p(t)$ into 20 side-by-side pillars of equal width. Thus, plume horizontal resolution is very fine in the very fresh plume (typically, ~ 20m), and gradually relaxes to approach the background pillar resolution (1.5 km) in the aged plume (plume width ~ 30 km). Vertically, plume core (= initial plume thickness at the end of the plume rise stage) is divided into a selected fixed number of thin layers (typically about 20m in thickness each), and as the plume expands, it does so sequentially into the adjacent layers of the plume slab.

In a typical simulation, the background (in the mixing layer and aloft) is initialized at 0600, and is subsequently evolved dynamically (physics) and kinetically (emissions, chemistry and removal). The background slab simulation is arranged to pass the point-source plume release location at the desired plume release time. The plume slab is then initialized 15 minutes after plume release time at the appropriate downwind location. At such initialization, the plume cross-section is centered at the effective stack height of the emission, and has finite width and height (externally specified, based on the Plume Rise Module of our Plume Dynamics Model, PDM, which is described in Gillani and Godowitch, 1999). The plume emission mass of each species is injected into this finite plume area (on top of the underlying background concentration field) in an assumed initial 2-D Gaussian distribution, calculated using input values of the species emission rate and the current local wind speed. The NO_x emission is assumed to be as NO. The distributions then evolve as the plume is advected along its pre-calculated trajectory (from the PDM run), under the influence of the various physical-chemical processes identified above. The model requires several inputs related to these processes: e.g., point-source and surface emissions; the dynamic mixing height $[z_i(t)]$ and plume width and height $[W_p(t), H_p(t)]$; diffusion parameters; the j-values of the photolytic species; the deposition velocities (v_d) of the depositing species; meteorological variables, p, T, RH; etc. These inputs may be empirical or semi-empirical, (calculated based on parameterizations available in PDM), or some of them may be derived from larger-scale grid model results (e.g., p, T, RH, Z_i, J, etc.). More specific information about particular model inputs for the case study are given in the following sections.

4.2 Multi-plume Version

Large coal-fired power plants operated by large utilities in the US typically emit between 10K and 100K tons of NOx (as NO_2)per year, or about 25 to 250 kmoles(NO)/h. By comparison, the largest sources of NOx in the H-G ship channel complex (SCC) emit about 25-50 kmoles(NO)/h. Some of them are power plants (negligible VOC emissions), but most co-emit both NOx and VOC. There are a large number of major industrial point sources (IPSs) in the SCC. Within a fairly short distance downwind of the SCC, the plumes of these sources begin to merge; some of these plumes are totally embedded in larger plumes emitted upwind. The treatment of such multiple interacting plumes is a complex challenge, particularly in the context of a *plume* model such as UAH-LRPM, with a rather fine spatial resolution (say, 200 m or finer horizontally) in the near-source downwind stretch where the plume merging is occuring. As shown in Fig. 1, most of the IPSs are concentrated in five clusters or local complexes --- three relatively small and more or less isolated ones, viz., Sweeney, Freeport and Chocolate Bayou in the south of the H-G area, and two (Texas City and the SCC), which are larger and tend to interact with each other. SCC is by far the largest complex with more than 100 individual IPSs of significant size. We have modified the single plume version of UAH-LRPM specifically for this project, to create a new multi-plume version (M-LRPM).

Conceptually, our approach in multiplume modeling is to initialize the plume slab just downwind of the most upwind source in the complex, then simulate its processes during downwind transport past the next source downwind until the new source has reached a certain minimum width (we have chosen that as 2 km). At that point, if there is physical interaction between the two plumes (based on overlap of their widths), then the plume slab is reinitialized, with the two plumes merged into a new single inhomogeneous plume with two concentration modes of the primary emission species. The merged plume has a new geometry, pillar configuration, spatial

resolution, and rate of growth, as well as a new merged concentration distribution of the transported species (free radical species adjust rapidly to a new equilibrium with the new distribution of the transported species). The new plume is then transported and evolved downwind until it interacts with the next downwind plume which is at least 2 km wide. If so, then these interacting plumes are merged and the simulation is re-initialized and resumed. This process is continued (i.e., reinitialization of the master plume at each new interaction) until all plumes in the complex have been accommodated in the master plume simulation. Thereafter, the simulation of the combined (master) plume is continued to the end of the prescribed simulation time and location.

In practice, a new plume physics preprocessor to M-LRPM was developed and implemented, which uses PDM to perform the dynamics of each individual plume in the complex independently, determines when plume interactions occur and the criteria for merging are met. It sets up flags to indicate when particular identified plumes are ready to be merged. M-LRPM thus receives its multi-plume dynamics and merging information from the preprocessor outputs. When a plumes-merge is flagged, M-LRPM picks up the plume dynamics and merge information, rechecks the merge criteria, and if satisfied, performs the actual merge (re-initialization of the merged plume), and then proceeds forward with the simulation of the merged plume.

One important practical issue to contend with in such multi-plume simulation is that when two plumes of different ages and stages of development interact and are flagged as ready for merge, they will have different spatial resolutions. Our approach is to limit maximum plume cell size (horizontally) to 200 m during the merge phase; at merge time, the new resolution of the merged plume is set at the coarser of the two individual plume resolutions, or 200m, whichever is smaller (remember that the newer of the two plumes will have a resolution of at least 100m before merge, because of the merge criterion that each member plume to be merged must be at least 2 km wide, and because each isolated plume has 20 pillars before it is merged). One problem in this process is that fairly fresh plumes (of width comparable to, or less than, the turbulent eddy scale) have a lateral diffusion rate which is different from that of a more aged plume in which turbulent eddies are significantly smaller than plume dimension, and merely perform internal plume diffusion. When two such diverse plumes are merged, the model limitation of a single lateral diffusivity for the whole plume (that of the larger member) leads to somewhat excessive post-merging diffusion of the younger member plume. This is one of the limitations of our approach. This is the reason that we require each merging plume member to be at least 2 km wide, so that it has already spread to a width which is larger than the turbulent eddy scale. Thus, if the smaller plume is embedded within the larger plume at its emission, then it will be simulated as an isolated plume until it is 2 km wide. While this will introduce some error, we do not think that such error will be too large in the total scheme of things. Two better approaches for simulation of plume-plume interactions, both requiring MUCH more computation, are the LES approach (Eulerian) and the *puff* modeling approach (Lagrangian) with fine spatial resolution (e.g., with the requirement that puffs are split up when they reach some critical size, e.g., 200 m). Both of these approaches also have the advantage that they can naturally and explicitly simulate wind shear effects. However, using either of those approaches remains a future project.

5. SELECTION OF INDUSTRIAL POINT SOURCES FOR SIMULATION

The H-G area has a very large number of industrial point sources. Even the high-resolution aircraft data cannot resolve all of their plumes. Figure 3 shows maps of the location and emission size of the largest (by emission) 200 point sources of NOx (Fig. 3a) and of OLE (Fig. 3b), where OLE is the aggregated class of olefins simulated as a group in the CB4 chemical mechanism, which we have used in all our simulations. It includes all alkenes other than ethene, which is treated separately and explicitly in CB4. Nearly 80% of the OLE emissions are, typically, as propene. Effectively, OLE represents the propene-equivalent concentration of all alkenes other than ethene, and is heavily dominated in the Houston IPSs by propene. For modeling and top-down emissions verification, we need to aggregate the sources to a manageable number. We went through a process of performing such aggregation of all major point sources (MPSs) in the five VOC emission clusters shown in Fig. 1, using the emissions inventory information supplied by the Texas Commission for Environmental Quality (TCEQ). The most important criterion in such aggregation, of course, was the proximity of the sources. We first aggregated all sources within 1 km of each other, and then did further aggregation by a manual examination process, finally resulting in a total of 35 composited (aggregated) sources: the sources at Sweeny were combined into a single aggregate point source; those at Freeport into three (Freeport A, B and a source in between them); those at Chocolate Bayou into two, and those in the Texas City and Ship Channel complexes into 29. These 35 sources are shown in Figure 4 (Fig. 4a shows the locations of the sources and a measure of their NOx emissions, and Fig. 4b shows the same for a measure of the OLE emissions). Figure 5 shows the 29 aggregated sources of the Texas City-SCC group in a more detailed plot, showing the sources numbered individually. Our diagnostic model-data analyses aimed to resolve each of these 35 sources individually, and to come up with diagnostic estimates of NOx and VOC emissions from each of these aggregated sources.

6. THE METEOROLOGICAL SCENARIO FOR THE CASE STUDY (28 Aug 2000)

Figure 2 showed the five IPS clusters, the NCAR Electra flight path (~1200 – 1800 CST), the measured ozone concentration distribution (mostly in the boundary layer) along the flight path (hence also the plume locations), and the approximate plume trajectories from the emission sources. The figure showed graphically that the winds were sustained throughout the daytime from the S-SE direction. Figure 6 shows the map of the H-G area and the aircraft flight path, along with locations of met monitoring sites. Along the aircraft flight path, aircraft locations are shown at half-hour intervals, the nine separate traverses are delineated as T1 – T9, and segments where the aircraft was either ascending or descending (usually where the aircraft was making a turn) are highlighted (in color). The data from these segments have been used to infer continuous vertical soundings or distributions of the measured variables. There were five met monitoring sites with 915 MHz wind profilers (Houston SW [Hsw], Elligton Field [Ell], LaMarque [LaM], Wharton [Wha] and Liberty [Lib]), two sites with radiosondes (Wharton [Wha] and Downtown [Dntn]), and two sites with met towers (Downtown [Dntn] and LaPorte [LaP]). These various datasets collectively provided vital meteorological information related to transport winds and mixing heights. In addition, very useful continuous spatial distribution of mixed layer height information was also deduced from the remote-sensing UV-DIAL data (vertical profiles of ozone

and aerosol backscatter) from the NOAA-ETL lidar aircraft. Also, very vital information related to actual plume transport trajectories of the sampled and simulated plumes could be inferred from the *in situ* aircraft chemistry data (e.g., the ozone data shown in Fig. 2). Finally, information about cloud fields and solar insolation (for use, especially, in the calculation of photolysis rates) was derived from the GOES-8 geostationary satellite data.

On August 28, the flow was onshore all day (Figure 7). The winds were generally southerly onshore in the morning, turning to a SE direction later. The trajectory shown is based on the profiler data. A sampling of the hourly profiler data (vertical wind profiles) at Ellington, Wharton and Liberty are presented in Figure 8. The wind data from these three profilers were available to us during the period of our analyses, and provided the wind speed information, in particular, which was of critical importance in plume dynamics calculations and in the initialization of plume concentrations of the primary emission species. We adjusted the profiler wind directions a little, as necessary, to ensure that the target plumes arrived at the correct aircraft sampling locations as inferred from the aircraft data (e.g., Fig. 2).

Mixed layer height is a critical parameter in air quality modeling. Particularly during onshore flow, the Houston area is characterized by a considerable spatial variability of mixed layer depth due to its coastal location and due to variations in land use (Senff et al., 2002). The gradients are particularly sharp near the land-sea interface, as shown in Figure 9, based on continuous aircraft lidar data of aerosol backscatter. The aircraft lidar data are particularly useful in providing such snapshot information about the spatial variability of mixed layer depth (Z_i). Figures 10, 11 and 12 collectively show such data in segments, which together make up the whole flight of the NOAA-ETL lidar aircraft, lasting about the same time period (~1200 – 1800 CST) as that of the flight of the NCAR Electra. These figures depict in detail the spatial distribution of Z_i over the study area for the case study timeframe. Whereas the lidar aircraft data provide excellent snapshots of the *spatial* (horizontal) distribution of Z_i, the profiler data at specific sites provide good local information about its *temporal* variation. Figure 13 provides such temporal variation of Z_i based on the profiler data at the Houston Southwest inland site. It clearly shows the growth of the mixing layer from 0800 to 1400 CST, reaching a peak height of about 2000m AGL at 1400 CST, and its subsequent fall-off after 1600 CST (2200 UT). Figure 14 shows the temporal variations of Z_i at all five profiler sites. Figure 15 shows results of vertical soundings of ambient temperature (T), dew point temperature (T_d), relative humidity (RH) and specific humidity (q) for the radiosondes at the Downtown and Wharton sites, with delineation (red dashed lines) of the base of the elevated inversions (Z_i). Figure 16 shows results of vertical soundings of T and RH, as well as of NO_y and O_3, for aircraft soundings at locations V_i (i = 1, 2, 3), which are shown in Figs. 6 and 17, again with delineation (dashed lines) of the elevated inversions. There was a good degree of agreement in these variety of mixing height data, which were used in determining the corresponding model inputs.

Senff et al. (2002) performed an analysis of the mixing height data of both the lidar aircraft and of the profilers for this case study day. The following description is based on their analysis. Due to the persistent onshore flow all day, the evolution of mixing height was strongly influenced by advection of marine air from the Gulf of Mexico and Galveston Bay. The data show a significant SE-to-NW gradient in mixing height, which increased with distance from the shore. The peak mixing height at LaMarque (near shore) was significantly lower than that at Ellington (somewhat inland) which, in turn, was lower than that at Houston SW (farther inland, Fig. 14). The lidar

measurements from the first portion of the flight (12:06 – 13:15 CST, Figure 10) clearly support this assessment. Low mixing depths of 400 to 800 m were found over the Gulf of Mexico and the northern end of Galveston Bay, while mixing depths of around 2000 m were measured west and northwest of downtown Houston. The lidar measurements from the second part of the flight (13:15 – 15:11 CST, figure 11) confirm the existence of strong spatial gradients in mixing depth in the vicinity of Galveston Bay. Over a distance of about 40 km to the west and northwest of the Baytown and La Porte areas the mixing depth increased by up to 1500 m. North of the Houston urban area, the lidar data show a localized enhancement of the boundary layer depth with peak values reaching, and even exceeding, 2500 m (Fig. 12). This appears to indicate that a deeper boundary layer developed over the Houston urban area and was transported to the north by the large-scale onshore flow. During the remainder of the flight (15:15 – 18:00 CST, figure 12), the airborne lidar mapped out the Houston urban and Ship Channel pollution plume that had been transported to the vicinity of Conroe. It appears that the influence of the marine air advected by the onshore flow did not reach that far north, allowing the mixed layer there to grow to depths of up to 2800 m. In our diagnostic modeling, we have tried to incorporate such observed variabilities in mixing depths as accurately as possible.

7. MEASURED AND MODELED PHOTOLYSIS RATES

Figure 17 shows a map of cloudiness in the study area at midday on August 28, based on GOES-8 data related to surface insolation. There were only light scattered clouds in the area on this day. We have used such satellite-based cloud and insolation information in the calculation of species photolysis rates used in the chemical modeling. Vertical profiles of the aircraft-measured values of the photolysis rate of NO_2 (J_{NO2}) at locations J_i (i = 1- 4) are also used in this study to check those calculated in the regional models CAMx and CMAQ. Figure 18 shows a comparison of the measured (in the Electra) photolysis rates of NO_2 (J_{NO2}) at aircraft locations J_i, i = 1,2,3,4 (shown in Figs. 6 and 17) and the corresponding *clear-sky* values calculated in the models CAMx and Models3-CMAQ. The measured data show decreased values related to attenuation by clouds, but these measurements were mostly under fairly clear sky. The data-model comparisons indicate that the CAMx clear-sky values compare very well with the measured clear-sky values; the calculated CMAQ clear-sky values are somewhat lower, with the error increasing with height, and approaching 10% at 3 km. For our model input of J-values for all photolytic species, we started with the CAMx-calculated tabulations of the clear-sky values (available at 4 km horizontal grid resolution and the CAMx vertical resolution), and then attenuated these locally using GOES-8 observed surface insolation data (available at 1 km horizontal resolution).

8. RESULTS OF THE DIAGNOSTIC DATA ANALYSES

8.1 The Isolated Southern Complexes: Sweeny, Freeport and Chocolate Bayou

Figure 19 (left panels) shows the southern part of the study domain, the corresponding largest sources of NOx, OLE and ETH (top to bottom, respectively), the southernmost and earliest three traverses (T1, T2, T3) of the NCAR Electra and, in the center panel, the approximate trajectories

of the plumes from the Sweeny, Freeport, Chocolate Bayou and Texas City complexes which were encountered in these traverses. We performed a diagnostic analysis (model-data comparisons) of each of these sampled plumes in each traverse. We present here four selections out of these analyses (these four selected sampled plume locations are shown as solid blue round symbols along the traverses in the left center panel), viz., the Sweeny plume sampled along T2 and T3, the Freeport plume along T2, and the Bayou plume along T3. The right panels in Figure 19 show the Electra continuous data traces for NOy and ozone along traverses T1, T2 and T3 (respectively, from bottom to top), along with identification of the four selected plumes (solid blue round symbols). As can be seen, each of these plumes is isolated from the others. A separate analysis will be presented in the next section, for the sampled plumes from the Texas City and the Ship Channel complexes, because the plumes from these sources became fused and required more complex modeling and diagnosis. In our analyses, as stated before, the Sweeny industrial point sources were combined into a single composite source, the Freeport sources were combined into three composited sources (Freeport A, Freeport B, and a composite source in the middle, which we will call Freeport M), and the Bayou sources were aggregated into two composite sources.

The correct simulation of plume dynamics is of critical importance in the simulation of nonlinear plume chemistry. Figure 20 illustrates our approach in performing the plume dynamics simulations, and (very importantly) in the selection of input data for these simulations. The plume dynamics simulations are performed with our Plume Dynamics Model, PDM (Gillani and Godowich, 1999), which uses a detailed particle model to perform the plume trajectory calculations, and the rest of the model to perform plume rise and spread calculations. PDM is configured to use empirical input data as much as available, and regional model inputs otherwise. The left and right panels (Fig. 20), respectively, show some results of plume trajectory calculations for the Sweeny plume sampled in traverses T2 and T3. The Sweeny plume in traverse T2 (left panel) was sampled at about 1312 (decimal 13.20), and in traverse T3 at about 1356 (decimal 13.94). The release time for each of these sampled plumes was estimated by doing back trajectories using the available wind data. In each case, we had profiler wind data available for the Ellington, Wharton and Liberty sites, at distances from Sweeny of ~82, 100, 150+ km, respectively, and we ran back trajectories for the following combination of the profiler data: Ellington only (E), Ellington and Wharton (EW), and all three sites (EWL). Different plume release times were deduced for each of these data combinations (11.50 ± 0.33h for the T2 plume, and 10.17 ± 0.50h for the T3 plume). Then, we ran forward trajectories from Sweeny, each starting at the appropriate release time, and all ending at the same sampling time (~13.20 for T2 and ~13.94 for T3). These separate plume transport trajectories are shown in the figure (three in each panel). Their arrival locations are reasonably close to the actual sampled location. Based on more detailed considerations, we ended up selecting the profiler combination EW for all our analyses of these southern "isolated" plumes. Corresponding to these, the plume transport times were calculated as ~ 1.67h for T2 (at an average transport speed of 3.8 m/s) and ~ 3.75h for T3 (at an average transport speed of 3.7 m/s). In the actual analyses, we modified the wind directions in the simulations slightly to make the trajectory end points coincide exactly with observed plume core. Another meteorological variable which is very important in chemistry simulations is the wind speed at effective stack height at the time of plume chemistry initialization, U_0. The initial concentration distributions in the plume for the emitted species are inversely proportional to this variable. It thus directly influences the downwind concentrations

of the primary species (NOy, ETH, OLE) which are compared to the corresponding measured concentrations to infer the emission rates of these species. Thus, the uncertainty in this variable translates in direct proportion to that introduced in the inferred "corrected" emission rates. Our estimates for U_0 at the calculated effective stack heights at plume initialization times, based on EW winds, were 4.6 m/s for the T2 Sweeny plume and 5.3 m/s for the T3 Sweeny plume. Finally, another variable which directly affects these concentrations is the mixing height variation with time during plume transport. For all the southern plume simulations, we have used the variation which is approximately as shown in Fig. 13, peaking at 1900m at 1400 CST (2000 UT). For comparison of these met inputs in plume simulations, the more simplified simulations in Trainer et al. (2001) used a constant (in space and time) wind speed of 4 m/s and a constant (in space and time) mixing height of 1500 m. As for plume spread, we also adjusted our mixing parameters such that the simulated plume spread closely matched the corresponding observed plume spread.

Figure 21 illustrates the procedure by which we diagnosed the effective emission rate of NOx for the Sweeny plume in T2. The simulated concentration profiles of the NOy species (NOy, NOx, NOz) in the upper panels are for the emission inventory value of Q_{NOx}, i.e., $Q_{NOx}(EI)$, and these profiles clearly indicate a significant deficit compared to the corresponding measured concentrations. The simulated profiles in the lower panels show a much better simulation of the observed profiles, and were obtained using $Q_{NOx} = 1.66\ Q_{NOx}(EI)$. Trainer et al. (2001), by contrast, had estimated it to be $1.07\ Q_{NOx}(EI)$. This is reasonably consistent with our estimate, considering their 15% higher value of the initial NOx concentration (based on $U_0 = 4$ m/s compared to our 4.6 m/s), and their higher modeled NOx concentration at measurement time for a lower mixing height of 1500 m (compared to ours of 1900 m, a factor of 27% higher). We conclude, therefore, that within the uncertainty of the simulations and the observations, the actual NOx emission rate was probably significantly higher than the EI value, but definitely within a factor of 2. The simulations shown in Fig. 21 (upper) used the EI values for the emission rates of ETH and OLE also, and inferred or corrected values for ETH and OLE in the lower plots, these latter corrections having been made as follows. When we compared the corresponding model-data profiles of ETH, OLE (actually, single point measurements only for ETH and OLE), ozone, "PAN" (= NOz – HNO3) and FORM (measured formaldehyde + aldehydes, and simulated FORM in CB4), we found all the simulated values to be gross underestimates. We, therefore, iteratively increased the emission rates of ETH and OLE until we obtained a good comparison of the measured and simulated values of these VOC-sensitive variables. Figure 22 shows the corresponding comparison of our simulated ("corrected") and measured values for all these variables which are very sensitive to emissions of ETH and OLE. The simulations in this figure required $Q_{ETH} = 3.6\ Q_{NOx}$ and $Q_{OLE} = 2.0\ Q_{NOx}$, where $Q_{NOx} = 1.66\ Q_{NOx}(EI)$. The factors 3.6 and 2.0 are consistent with those inferred by Trainer et al. (2001); however, since our inferred Q_{NOx} is about 55% higher than theirs, so are our inferred values of Q_{ETH} and Q_{OLE}. As we have seen, these differences between their and our inferred values is a result mostly related to the input values of the met variables and model differences. It may also be noted that these inferred values of the emission rates for ETH and OLE are about 2 orders of magnitude greater than their EI values, and in this conclusion, the two analyses (ours and Trainer's), are quite consistent. Thus, our independent analyses are consistent in the order of magnitude scale of the conclusion about the VOC emissions, and the differences are within the factor of 2 type of scale, which characterizes the difference in our two analyses for the inferred emission rate of NOx.

We get a qualitatively very similar result for the diagnostic analysis of the Sweeny plume of T3, presented in Figure 23. Again, it shows the data-model comparison *after* we had made the adjustments to the input values of the emission rates of NOx, ETH and OLE (as described above for T2). There were no measurements this time of ETH and OLE in this plume, and so the comparisons are for NOy, ozone, PAN and FORM only, and are seen to be again reasonably good. They were obtained for inferred values of the primary emissions as follows: $Q_{ETH} = 3.6$ Q_{NOx} and $Q_{OLE} = 2.0$ Q_{NOx}, where $Q_{NOx} = 1.25$ $Q_{NOx}(EI)$.

Figure 24 shows the similar model-data comparison for the composite Freeport plume at T2 (~33 km downwind), and it is corresponding to inferred emission rates of the primary species as follows: $Q_{ETH} = Q_{NOx}$ and $Q_{OLE} = 0.2$ Q_{NOx}, where $Q_{NOx} = 2.0$ $Q_{NOx}(EI)$ for both Freeport A and M, and $Q_{ETH} = 1.5$ Q_{NOx} and $Q_{OLE} = Q_{NOx}$, where $Q_{NOx} = 1.5$ $Q_{NOx}(EI)$ for Freeport B. The analysis of Trainer had considered a single composite source for the whole Freeport complex (which they had called Freeport B), and their inferred values were $Q_{ETH} = 1.5$ Q_{NOx} and $Q_{OLE} = 0.5$ Q_{NOx}, where $Q_{NOx} = 0.97$ $Q_{NOx}(EI)$. Again, the two sets of results (ours and theirs) are consistent at the order of magnitude scale for the error in the VOC emissions, and within the factor of 2 kind of scale relevant to the uncertainty in the NOx emission rate.

Figure 25 shows the same for the Chocolate Bayou sources (two composite sources in our simulations). For the total Bayou source, our inferred emission rates are as follows: $Q_{ETH} = 4.0$ Q_{NOx} and $Q_{OLE} = 2.0$ Q_{NOx}, where $Q_{NOx} = 4.5$ $Q_{NOx}(EI)$. Trainer's study did not present any results for the Bayou complex. Note that our analysis suggests that the effective NOx emission rate of the total Bayou source is probably underestimated in the EI by as much as a factor of 4.5, well over the uncertainty, which we believe to be limited to a factor of 2.

What is consistent and important in all the results presented above for the southern sources is the fact that the EI emission rates of ETH and OLE are most probably grossly underestimated by about 2 orders of magnitude, and that the real emission rates of these species appear to be of the same order of magnitude as Q_{NOx}. It is also clear that when you combine such high rates of emission of the reactive species ETH and OLE with the type of NOx emissions from these sources, the standard gas-phase chemical mechanisms such as CB4 do indeed provide an adequate explanation for the observed high and rapid formation of ozone (and of aldehydes and PAN) that are observed in these industrial point source plumes, and that UAH-LRPM does simulate the observed compact spatial-temporal scales of the plumes. However, the simulated emission rates of these VOC species must be considered as upper bounds, since we have neglected the effects of the chemistry related to the turbulent fluctuations in the concentrations, which may well increase the reactions rates substantially, and therefore result in the observed chemistry for significantly lower VOC emissions. We suspect that the magnitude of this error may be of the factor of 2 type, rather than of the order of magnitude type. The question then is: how sensitive is such nonlinear VOC chemistry to the VOC emissions?

Figure 26 presents results of such a sensitivity analysis. It presents, for the Sweeny T3 scenario, the simulated concentration evolutions of the primary emission variables NOx, the propene-equivalent ETH+OLE, the ratio of the last two variables, and of the secondary variables OH, O3, FORM, HNO3 and "PAN" (the values are crosswind-profile average species concentrations at

the height of the aircraft traverse, about 600 m), to three sets of VOC emission rates, as follows: the red traces, marked EI, correspond to the EI values of the emission rates of ETH and OLE; the blue traces, marked EI+, correspond to ETH and OLE emission rates which are the same as the NOx emission rates; and, the black traces, marked EI++, are for $Q_{ETH} = 3.6\ Q_{NOx}$ and $Q_{OLE} = 2.0$ Q_{NOx}. Thus, the EI+ case involves VOC emissions which are about 2 *orders* of magnitude greater than the EI case, and the EI++ case involves a further increase in the VOC emissions by about a *factor* of 2-4. It is most instructive to interpret the sensitivities to the *ratio* VOC/NOx. We observe clearly that the formation of ozone, PAN and FORM is positively sensitive to the ratio VOC/NOx, and that the increased sensitivity to an increase in the ratio by a factor of 2-4 between the cases EI+ and EI++ is comparable to the increased sensitivity to an increase in the ratio by an order of magnitude of 2 between the cases EI and EI+. Thus, on an absolute basis, the sensitivity is greater in the range EI+ to EI++, than it is in the range EI to EI+. Thus, using the LES and accounting for the decreased emission rates of the VOCs (by including the effect of the turbulent chemistry) by perhaps something like a factor of 2, could have a quite large effect, since it will occur in the more sensitive range (EI+ to EI++). By contrast to the behavior of ozone, PAN and FORM, the behavior of OH and HNO3 is the opposite, except during near-field transport. The chemistry of these variables appears to be more NOx-limited in the mature plume, and VOC-limited only in the near field. This near-field regime is about 1-2 hours in duration (~ the time to recover the initial sharp depletion of OH by reaction with the high initial concentrations of both NOx and VOC), with this duration being correlated inversely with the VOC/NOx ratio. We now shift our attention to the analysis of the more complex multi-interacting plume behavior for the combined Texas City-Ship Channel complex.

8.2 The Multi-Interacting Plume Complex: Texas City and the Ship Channel

As shown in Figure 5, this complex of sources was aggregated into 29 composite sources, three in the Texas City area (the sources numbered 1, 2, 3, source #3 being a power plant), three more in the Ellington Field-LaPorte area (sources numbered 4, 5, 6) south of the Ship Channel Complex (SCC), 16 in the SCC (the sources numbered 7 through 22, source #21 being a power plant to the east of the SCC), and the remaining 7 sources (#23 – 29) situated to the north of the SCC. The emissions from all of these sources were sampled by the Electra during its traverses on 28 August 2000. We present here results of our diagnostic analysis (model-data comparison) of what was sampled by the Electra during the eastern legs of its traverses marked T5, T6, T7 and T8 in Figure 6, being respectively, about 10, 25, 50 and 75 km downwind of the Ship Channel.

Figures 27 and 28 pertain to the analysis for traverse T5, about 10 km downwind of the Ship Channel. In Figure 27, the model results are based on emissions of NOx and the VOCs as in the EI, and Figure 28 is based on emissions of NOx, OLE and ETH *after* iterative corrections to obtain our best match between the observed and simulated data. The analyzed part of the E-W traverse covered more than 50 km (horizontal axis in each panel) and the corresponding observed concentration profiles are the result of considerable interactions between the many industrial point-source plumes of the Texas City and Ship Channel complexes. Observe that the simulated profile reflects this admixed plume scenario well, capturing the detail in terms of the multiple NOx concentration modes. Each figure contains 12 panels, in three columns and four rows. The left column shows model-data crosswind concentration profiles of NOy, NOx, NO and NO2

14

from top to bottom, respectively; the second column shows the same for the secondary species O3, NOz, HNO3 and "PAN" = NOz-HNO3; and the final column shows the plots for the variables ETH, OLE, FORM and OH. No measurements were made of OH; throughout the whole traverse, only one single point measurement was made for ETH and OLE, and no valid measurements were available for FORM for this traverse. The data-model comparison of the primary N-species (column 1) shows that the simulated values are, in general, underestimates of the observed concentrations of these species, indicating that, in general, the NOx emissions must have been underestimated in the EI for most sources. This is particularly so for the sources in the western half of the traverse segment shown. The ETH and OLE single-point data show gross underestimation in the simulated VOC concentrations at the location of the single-point measurement. Ozone concentrations appear to be underestimated in the simulations in the left half of the profile, while HNO3 is considerably overestimated in the simulation in the right half of the profile. Figure 28 shows the results *after* both NOx and VOC emissions were iteratively adjusted for all sources: the NOy comparison is now good, as is that of ozone; the simulated values of ETH and OLE are also much closer to the observed values, but significant discrepancy persists there, as also in the simulation of HNO3. The extremely sparse observed data for ETH and OLE underscore the hazards in trying to match that single point for a very inhomogeneous profile so close to the sources. The absence of measured FORM data is sorely missed here, as it is very useful diagnostic information to infer VOC emissions, as we shall see later for traverses where it is available. The ozone data at this short downwind distance, being the result of depletions and productions in a mixture of plumes of various chemical ages, are also not ideal for the purpose of inferring the accuracy of the VOC emissions. The general conclusion here is that the available data are inadequate to deduce, with much confidence, the ETH and OLE emission rates from the observations of this profile alone. We badly need a more continuous dataset for ETH and OLE (such as was available in the data collected after 2000 in the Baylor Twin Otter). We proceed to explore the results of the analyses for the following traverses to throw more light.

Figures 29 and 30 present similar information for traverse T6, about 25 km downwind of the Ship Channel, Fig. 29 containing simulation results based on EI values of emission rates of NOx, ETH and OLE, and Fig. 30 containing simulation results after iterative "correction" of the emission rates of NOx, ETH and OLE. This time, there were two point measurements of ETH and OLE in this traverse, but fortunately, we have some more (yet only partial) data of FORM. Figure 29 shows again that for many of the point-source plumes sampled, the NOx and VOC emission rates appear to be significantly underestimated in the EI. Figure 30 is based on the same "corrected" emission rates of NOx, ETH and OLE as in Figure 28. The model-data comparison for NOy, ETH and OLE, as well as for ozone, FORM and the secondary N-species (column 2) are quite good, in general, except for a persisting overestimation in HNO3.

Figures 31 and 32 show similar plots, now for traverse T7, about 50 km downwind of the Ship Channel, Fig. 31 based on simulations with primary emissions as in the EI, and Fig. 32 with "corrected" primary emissions, the same as in Figs. 28 and 30. Once again, the comparisons in Fig. 31 show clearly significant underestimation in the primary emissions of both NOx and VOC, and those in Fig. 32 show much improved agreements for NOy, ETH, OLE, ozone and FORM; NOz appears to be somewhat overestimated in the simulation, mainly from PAN in the left half of the profile and from HNO3 in the right half.

15

Finally, Figures 33 and 34 show similar plots, now for traverse T8, about 75 km downwind of the Ship Channel, Fig. 33 based on simulations with primary emissions as in the EI, and Fig. 34 with "corrected" primary emissions, the same as in Figs. 28, 30 and 32. Once again, the comparisons in Fig. 33 show some underestimation in the primary emissions of both NOx and VOC, the discrepancy for VOC now being most clear in the secondary variables FORM and ozone. The comparisons in Fig. 34 show very good agreements for all variables except ETH and OLE, but this is not very surprising, for in such an aged set of plumes, ETH and OLE emissions are mostly depleted, and the measurements are close to their levels of detection. We emphasize that for all four traverses shown here, the "corrected" primary emissions of NOx, ETH and OLE are the same in the simulations for all four traverses. We have found generally that the simulations (with "corrected" ETH and OLE emission rates) do not provide good fits for both FORM and NOz; we have opted in favor of using those emission rates of ETH and OLE which provided best fits of observed ETH and OLE (except in the first and last traverses), as well as of observed ozone and FORM.

Table 1 summarizes the EI values of the emissions, as well as the "corrections" applied to NOx, ETH and OLE EI emission rates for each of the 29 sources included in the simulations shown in Figures 27-34. Information related to the EI emission rates (columns 2-6) is for NOx, ETH and OLE, as well as for ETH/NOx and OLE/NOx. For both of these ratios, the values are typically between 0.01 and 0.1. The next five columns show the same information after "correction". For most sources, no correction was made to the NOx emission rate. Upward corrections had to be applied to the NOx emission rates for sources # 8, 9, 10, 13, 15, 17, 19, 27 and 29 (see third column from the end); in particular, for sources # 9, 10, 13 and 17 (all in the left half of the SCC), the NOx emission rate had to be increases by at least a factor of 3. For most sources also, the *corrected* ETH/NOx and OLE/NOx ratios have the value 1 (columns 10,11), i.e., ETH and OLE corrected emission rates are similar to the corresponding NOx emission rates. Thus, the essential conclusion is same for these industrial point sources as for those in the isolated complexes (Sweeny, Freeport and Bayou): the NOx emission rates in the EI appear to be verified within a factor of 2 for most sources, but they appear to be underestimated by a factor of up to 5 for Bayou and a few SCC sources; and typically, the ETH and OLE emission rates appear to be underestimated in the EI by one to two orders of magnitude (last two columns in Table 1), and are rather comparable to the co-emitted NOx emission rates (colums 10, 11).

9. CONCLUSION AND RECOMMENDATIONS

9.1 Conclusions

A diagnostic analysis, based on comparison of aircraft observations in the H-G area as part of TexasAQS-2000 and Lagrangian reactive plume modeling using a state-of-the-art model upgraded for this project to simulate the evolving distributions of species concentrations in multiple interacting industrial point source plumes, has been carried out principally to infer the accuracy of the NOx and VOC emissions from these sources, and to test the abiility of lagrangian plume modeling for such purpose, has yielded the following major conclusions:

1. The industrial point sources in the H-G area are mostly concentrated in five complexes, three of which (Sweeny, Freeport and Chocolate Bayou) are more or less isolated, and the other two (Texas City and the Ship Channel Complex) have a fairly large number of sources in relatively close proximity such that their plumes tend to interact and form a mixed multi-plume complex.

2. For most of the sources, the NOx emission rates in the EI appear to be fairly accurate, most likely well within a factor of 2; there are some exceptions, however, specifically the Bayou sources and some sources in the western half of the SCC, for which the NOx emission rates appear to be a factor of 3 to 5 higher than their EI estimates.

3. Similarly, for almost all sources (except power plants), the ETH and OLE emission rates appear to be grossly underestimated in the EI, typically by 1 to 2 orders of magnitude, such that these emission rates are comparable to the co-emitted NOx emission rates. Such co-emissions of NOx and reactive VOCs lead to rapid nonlinear gas-phase chemistry, which produces large amounts of ozone and other secondary products (e.g., NOz, aldehydes) rather close to the source complexes, and appears to explain the development of THOEs observed before and during the TexasAQS-2000 study.

4. The CB4 chemical mechanism (and presumably also other state-of-the-art mechanisms, e.g., RADM2 and SAPRC99) is able to simulate the rapid observed chemistry adequately, making it unnecessary to invoke substantial contributions from other mechanisms such as chlorine chemistry which are not part of CB4 ordinarily.

5. UAH-LRPM and its upgraded multi-plume version (M-LRPM) are able to simulate the high-resolution observations of primary and secondary variables measured in the NCAR-Electra aircraft in the plumes of the H-G industrial point sources and their background. These models have performed very well as diagnostic tools to evaluate the EIs for these sources, and can be very useful also to perform a variety of other diagnostic tests (e.g., checking the relative differences between results of using different chemical mechanisms) for which regional or sub-regional Eulerian models would require much more intense resources. However, the LRPMs, and for that matter also the regional/sub-regional Eulerian models, can only provide upper-bound estimates of the inferred emissions, for they do not currently include the effects of the chemistry related to the turbulent fluctuations in the species concentrations.

6. To capture the turbulent fluctuating chemistry effects, the most reliable tool, in principle, would be very high resolution Eulerian Large Eddy Simulation models with detailed chemistry (LES-with-Chemistry). For the specific cases of large co-emissions of NOx and reactive VOCs, significant magnitudes of turbulent concentration co-variances may be expected to speed up the VOC-NOx chemistry significantly in the industrial point-source plumes, perhaps requiring correspondingly smaller emissions of these species to produce the observed chemistry than that inferred using the LRPMs or the regional models. LES-with-Chemistry, involving the full detailed chemical mechanisms such as CB4, is a brand new and more or less untested tool. Its applications, even without chemistry, has generally been limited to model domains limited to 10km x 10km horizontally in the CBL. For a complex

such as SCC, the meaningful domain size for such application would have to be more like 50 km x 20 km, and would require massive parallel processing on state-of-the-art computing systems. While such hardware systems are available, the corresponding multi-processing software for LES-with-Chemistry which can perform multi-point-source plume processes does not exist and needs to be developed. Under a current HARC-supported project, we are testing the application of LES-with-Chem to the Sweeny type of isolated industrial point source plumes in the H-G area.

7. The application of the LRPM has some physical limitations. In terms of plume dynamics, the LRPM is limited to applications under conditions when wind shear effects are not very significant, and also is not the ideal tool for simulation of multiple interacting plumes, because it cannot apply differing turbulent diffusion rates that may exist in different parts of the lagrangian air parcel including fresh and aged sub-plumes. To include such complex effects as wind shear and multi-plume interactions more realistically in lagrangian modeling, it would appear that the new EPRI puff model SCICHEM may be more suitable.

8. In terms of simulation of the gas-phase chemistry, our study has revealed a consistent overprediction of NOz (particularly HNO3) by CB4. This has also been observed in recent applications of CAMx with CB4 in the H-G area.

9. An important limitation of this study and of any diagnostic study for the H-G area aimed at top-down verification of the VOC and NOx EIs based on TexAQS-2000 database is the very sparse measurements of speciated VOCs (typically one point measurement in a 50 km aircraft traverse) in the Texas 2000 field study. There is a dire need for more continuous speciated VOC measurements, especially in the near-source regime. For example, continuous, or even semi-continuous measurements (as of the aldehydes), of the primary reactive VOCs (such as ethane and propene) in T5 of the Electra on the present case study day (28 Aug 2000) would have been invaluable in nailing down the inferred VOC emission rates from the SCC sources with much greater confidence. This capability is very much needed.

9.2   Recommendations

We wish to make four specific recommendations, as follows:

1. There is a need to perform LES-with-Chem diagnostic analyses of the industrial point-source plumes in the H-G area. This is on-going for the isolated plumes (e.g., Sweeny), but for its application to the complex SCC plume over a much larger domain, the present LES-with-Chem code needs to be upgraded for implementation in multi-processing mode on massive parallel computing hardware.

2. There is a need to test the applications of chemical mechanisms other than CB4 to simulate the chemistry of the H-G area, particularly with respect to simulation of NOz species, which appear to be consistently overpredicted by CB4. The LRPM is an ideal inexpensive tool for such tests.

3. The LRPM has important limitations with respect to realistically simulating such complex effects as significant wind shear and interacting multiple plumes with nonlinear chemistry. The case study day of the present study was an unusually simple scenario meteorologically. The application of Lagrangian modeling to scenarios with recirculations and much higher ozone production than on 28 Aug 2000 would be very useful to test effects related to fast chemistry in more intense ozone episodes. We recommend the application of SCICHEM for such applications. The satisfactory evaluation of SCICHEM has just been completed.

4. We recommend highly the application of UAH-LRPM to a similar case study for which higher density data are available of ethene and propene, such as the measurements made in the Baylor Twin Otter subsequent to the 2000 study.

10. **REFERENCES**

Breitenbach, P. (2002): Accelerated science evaluation of Houston ozone. Regional Air Quality Planning Committee presentation, March 21, 2002.

Carter W. P. L. (1996): Condensed atmospheric chemistry mechanisms for isoprene. *Atmos. Environ.* **24**, 4275-4290.

Daum, P. et al. (2002): Accelerated science evaluation of ozone formation in the Houston-Galveston area --- Summary, February 18, 2002.

EPA (1999) : <u>Science Algorithms of the EPA Models-3 CMAQ Modeling System</u>, EPA-600/R-99/030, Mar 1999..

Gillani, N. V. (1986): Ozone formation in pollutant plumes: Development and application of a reactive plume model with arbitrary crosswind resolution, EPA/600/S3-86-051.

Gillani, N.V. et al. (1998): The plume-in-grid treatment of major elevated point-source emissions in Models-3, Preprint Vol., AMS-AWMA Conf Air Poll. Met, Phoenix AZ, Jan. 1998.

Gillani N.V. and J. Godowich (1999): Plume-in-grid Treatment of Major Point Source Emissions", Ch. 9 in <u>Science Algorithms of the EPA Models-3 Community Multi-scale Air Quality (CMAQ) Modeling System</u> , EPA-600/R-99/030

Herwehe, J.A. et al. (2002): Initial application of a coupled LES-Photochemical model to examine near-source ozone production from industrial emissions. Paper presented at the 15th AMS Symp. on BL and Turb., Wageningen, Netherlands, July, 2002.

Pleim, J.E. and J.S. Chang (1992): A non-local closure model for vertical mixing in the convective boundary layer. *Atmos. Environ.* **26A,** 965-981.

Riemer, D.D. et al. (2000): Atomic chlorine is an oxidant in Houston, TX. AMS Meeting, Orlando.

Ryerson, T. et al. (2001): Contrasting effects of different anthropogenic source types on ozone formation in Houston. Paper presented at the Texas 2000 Air Quality Study Data Review Meeting, Austin TX, June 2001.

Senff, C. J. et al. (2001): 3-D distribution of ozone in the Houston area during the 8/29 – 9/6 pollution episode. Paper presented at the Texas 2000 Air Quality Study Data Review Meeting, Austin TX, June 2001.

Senff, C. J. et al. (2002): Spatial and temporal variations in mixing height in Houston, Preliminary Report of NOAA-ETL (Project F-20) to Texas Commission for Environmental Quality, 2002.

Tanaka, P.L. et al. (2000): Anthropogenic sources of chlorine and ozone formation in urban atmospheres. *ES&T* **34**, 4470-4473.

Tanaka, P.L. et al. (2001): Direct evidence for chlorine chemistry and assessment of its role in urban ozone formation. Submitted to *Science*.

TNRCC (2001a): Accelerated Science Evaluation of Ozone Formation in the Houston-Galveston Area --- Sep 2001.

TNRCC (2001b): Conceptual model for ozone formation in the H-G area. Appendix A to Protocol for Ozone Modeling of the H-G Area (Phase 1 of the 2004 Mid-course Review). 29 Oct 2001.

TNRCC (2002): Accelerated Science Evaluation of Ozone Formation in the Houston-Galveston Area --- Summary, 2/18/02.

Trainer, M. (2001): Are the observations made on the NCAR-Electra consistent with chemical processing ? Paper presented at the Texas 2000 Air Quality Study Data Review Meeting, Austin TX, June 2001.

Wood, R. (2002): Findings related to ozone formation events in the H-G non-attainment area… Memorandum to Commissioner's Work Session, 28 February, 2002.

TABLE 1. Data of EI and "Corrected" Emission Rates for the Industrial Point Sources in the Texas City and Ship Channel Complexes

Source #	EI Emission Rates, Qei (Kmol/h)					"Corrected" Emission Rates, Qc (Kmol/h)					Correction Ratios(Qc/Qei)		
	NOx	ETH	OLE	ETH/NOx	OLE/NOx	NOx	ETH	OLE	ETH/NOx	OLE/NOx	NOx	ETH	OLE
1	20.05	0.57	1.51	0.0285	0.0758	20.05	6.66	6.66	0.33	0.33	1	11.69	4.4
2	17.60	0.78	1.45	0.0442	0.0822	17.6	5.87	5.87	0.33	0.33	1	7.54	4.06
3	32.36	~	~	~	~	32.36	~	~	1	1	1	~	~
4	10.19	0.13	0.44	0.0127	0.0431	10.19	10.19	20.41	1	2	1	78.9	46.41
5	7.63	0.28	0.10	0.036	0.0125	7.63	7.63	7.63	1	1	1	27.72	79.76
6	4.64	0.14	0.08	0.0293	0.0158	4.64	4.64	15.3	1	1	1	34.21	200.81
7	~	~	~	~	~	~	~	~	1	1	1	~	~
8	8.35	1.36	0.44	0.1626	0.0532	16.7	16.7	33.41	1	2	2	12.3	75.15
9	15.52	1.14	0.70	0.0732	0.0451	46.55	46.55	46.55	1	1	3	41.01	66.46
10	12.87	0.38	0.79	0.0367	0.0611	51.48	51.48	64.33	1	1.25	4	136.08	81.88
11	~	~	~	~	~	~	~	~	1	1	1	~	~
12	~	~	~	~	~	~	~	~	1	1	1	~	~
13	10.55	0.48	1.23	0.0453	0.1165	31.64	31.64	31.64	1	1	3	66.25	25.75
14	~	~	~	~	~	~	~	~	1	1	1	~	~
15	7.99	0.31	0.73	0.3819	0.0911	15.98	15.98	15.98	1	1	2	52.37	21.95
16	1.54	~	0.78	0.0251	0.506	1.54	~	0.78	0.0251	0.506	1	1	1
17	6.91	0.13	0.16	0.0181	0.0354	34.56	34.56	34.56	1	1	5	275.51	211.61
18	~	~	~	~	~	~	~	~	1	1	1	~	~
19	5.42	0.07	0.20	0.0132	0.0368	10.84	10.84	10.84	1	1	2	151.2	54.33
20	1.46	~	~	0.0429	0.184	1.46	~	~	0.0429	0.184	1	1	1
21	15.95	~	~	~	~	15.95	~	~	1	1	1	~	~
22	15.23	0.33	0.65	0.0217	0.0425	15.23	15.23	15.23	1	1	1	46.15	23.5
23	~	~	~	~	~	~	~	~	1	1	1	~	~
24	4.39	0.25	0.04	0.0571	0.0101	4.39	44.06	17.64	10	4	1	175.28	395.16
25	7.74	~	~	~	~	7.74	~	~	1	1	1	~	~
26	~	0.13	0.00	~	~	~	72.72	22.03	~	~	~	546.15	7802.5
27	21.15	1.07	2.59	0.0504	0.1223	31.72	31.72	31.72	1	1	1.5	29.75	12.27
28	~	0.38	~	16.7	0.869	~	0.38	~	16.7	0.869	1	1	1
29	2.79	0.28	0.22	0.0183	0.001	5.58	27.94	22.36	5	4	2	100	100

~ = small
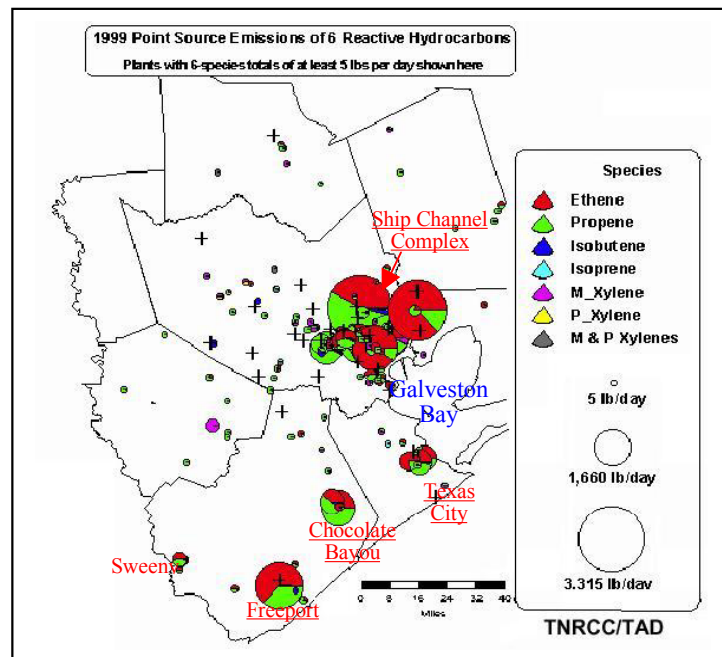
Figure 1. Map of the H-G area showing the major clusters of industrial point sources (IPSs).
(Based on VOC emissions inventory)
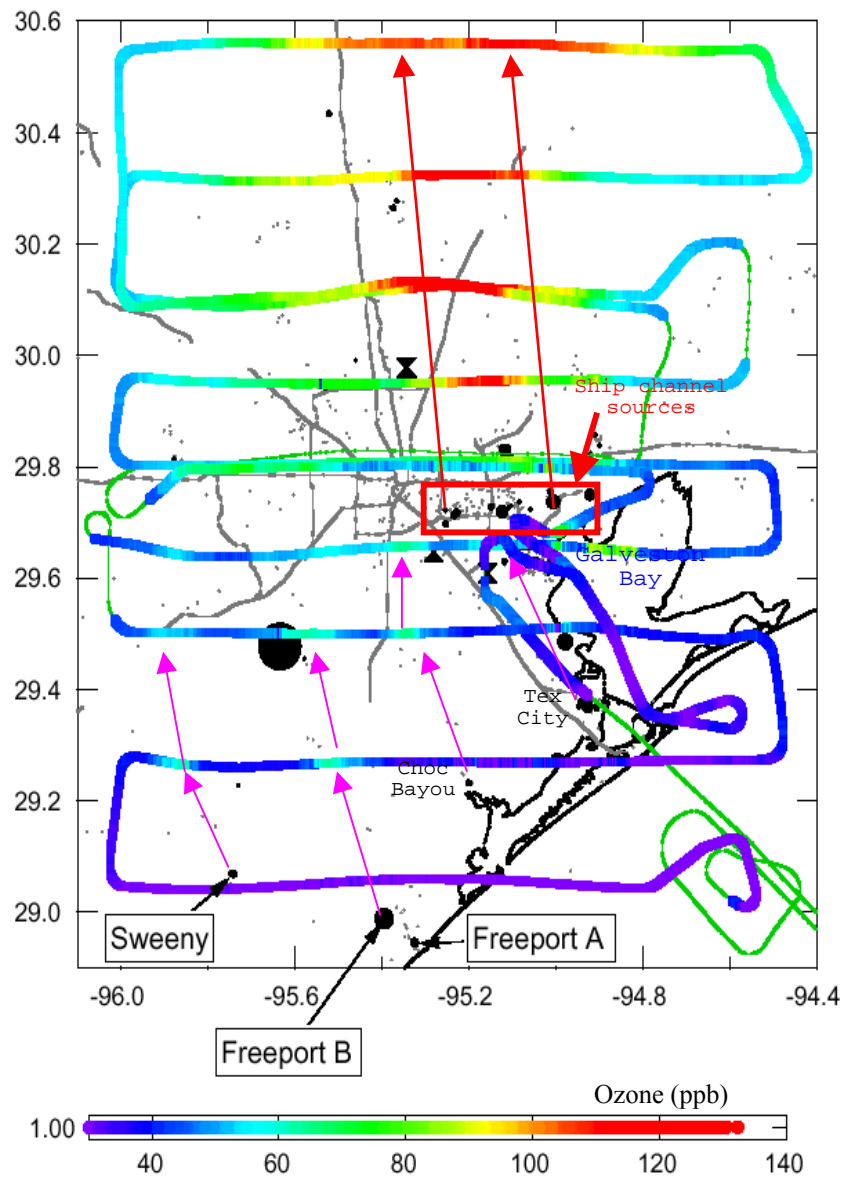
Figure 2. Map of the H-G area showing the flight path of the NCAR Electra aircraft mission of 28 Aug 2000. The color coding along the flight path shows measured ozone concentration distribution along the path. Approximate plume trajectories for emissions from the main industrial point source clusters are also shown by arrows downwind of the clusters. (Base plot taken from Trainer et al., 2001; some additional information also included)
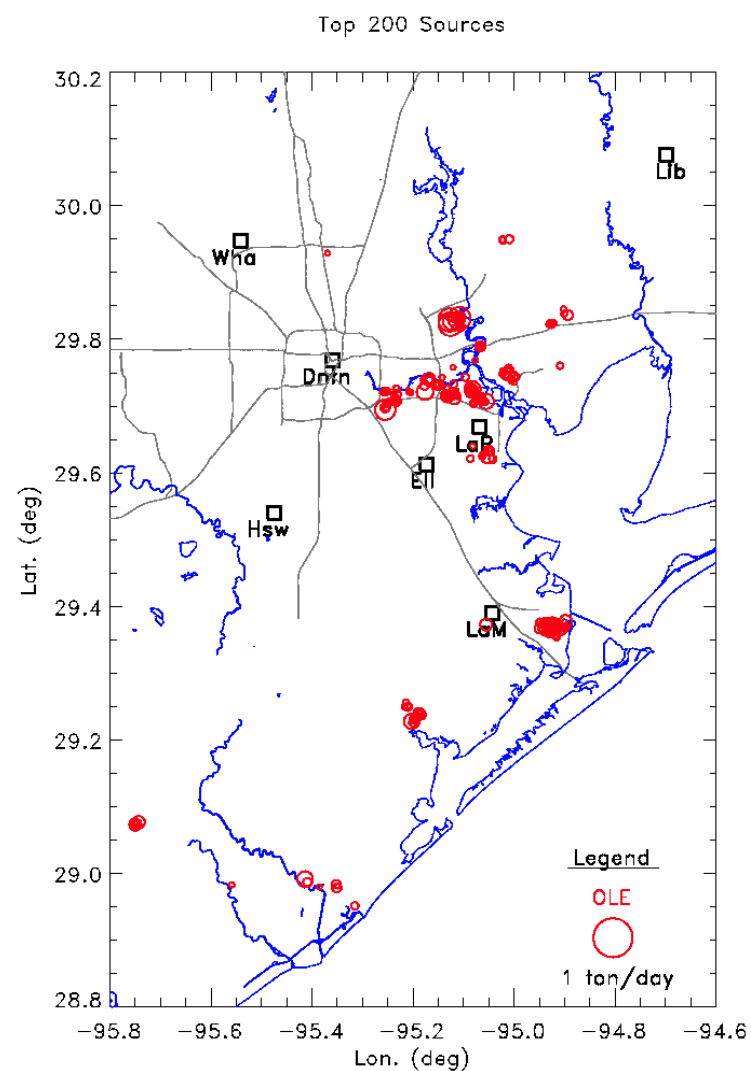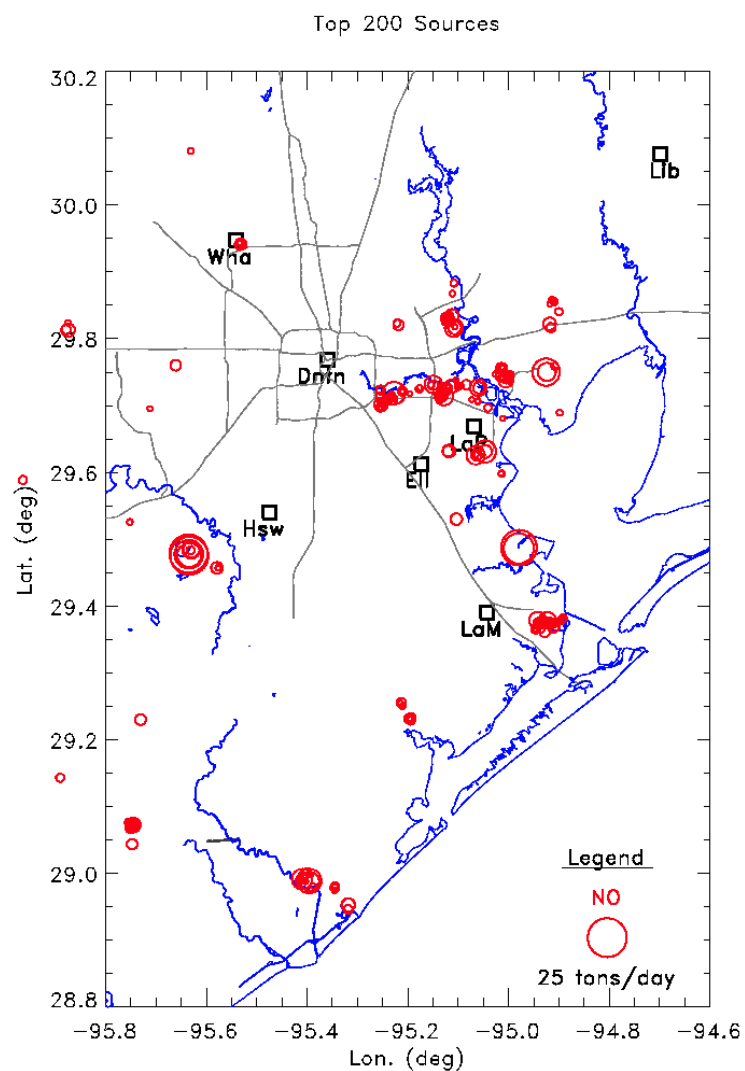
Figure 3. Locations and daily emission rates of the largest 200 major point sources of NO (Fig. 3a, left) and of OLE (Fig. 3b, right). OLE represents the grouped class of alkenes other than ethane in the CB4 chemical mechanism.. Observe the clustering of the OLE sources in the following five locations (see Fig. 2): Sweeny, Freeport, Choc. Bayou, Texas City and the Ship Channel Complex.
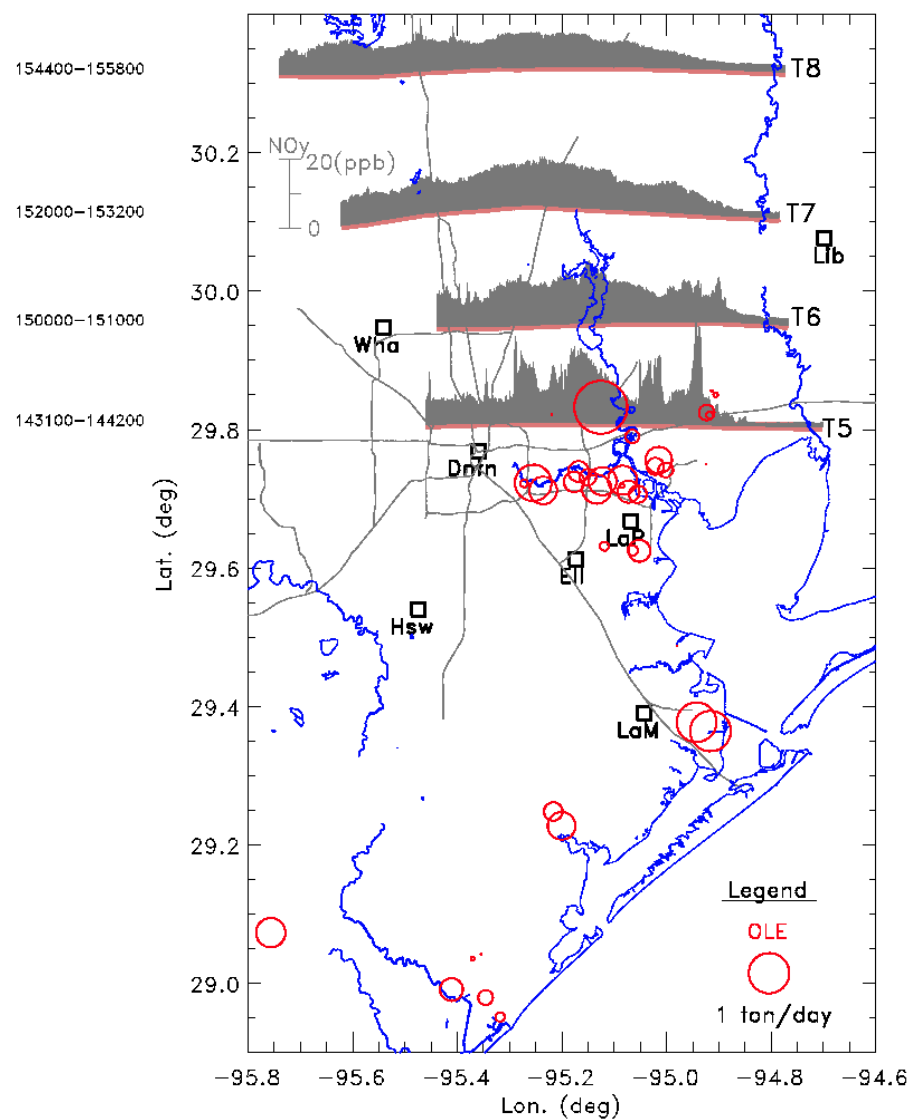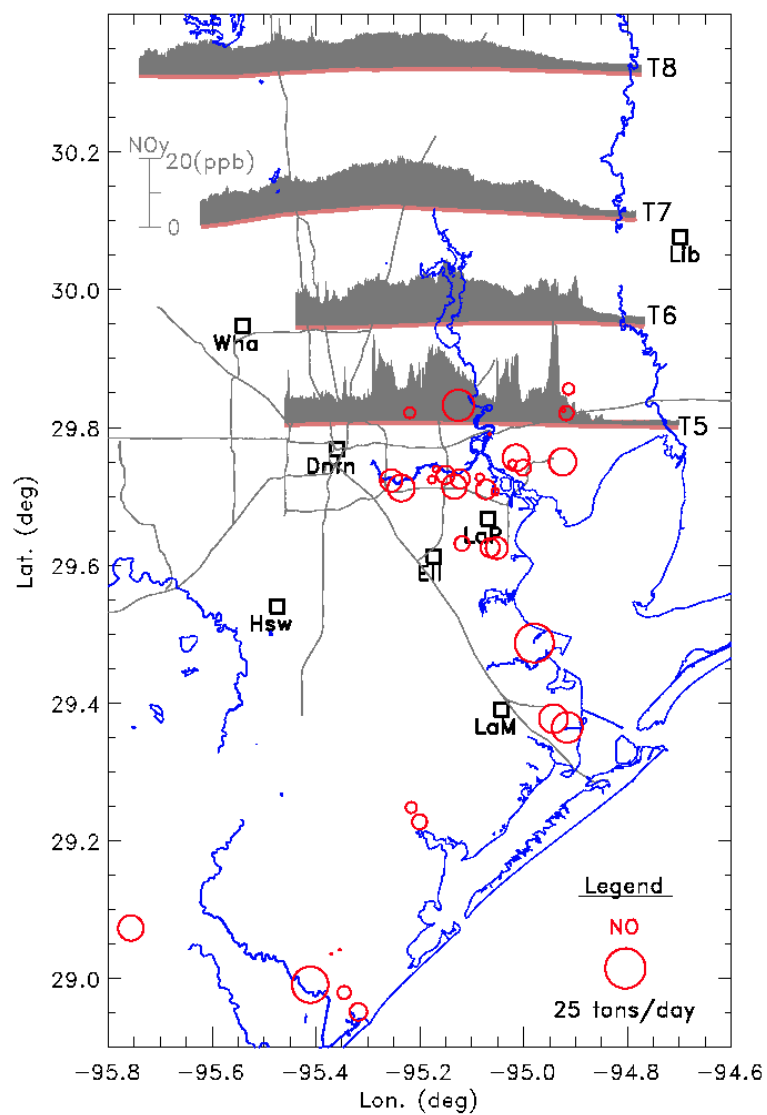
Figure 4. Locations and daily emission rates of NO (Fig. 4a, left) and of OLE (Fig. 4b, right) for the 35 "aggregate" major point sources for which plume dynamics and chemistry simulations have been performed in the present diagnostic analysis.
The distribution of these sources is as follows: Sweeny (1), Freeport (3), Choc. Bayou (2), Texas City and the Ship Channel Complex (29).
The maps also show the NOy concentration profiles as measured during four cross-plume traverses downwind of the Ship Channel Complex by the NCAR Electra aircraft.
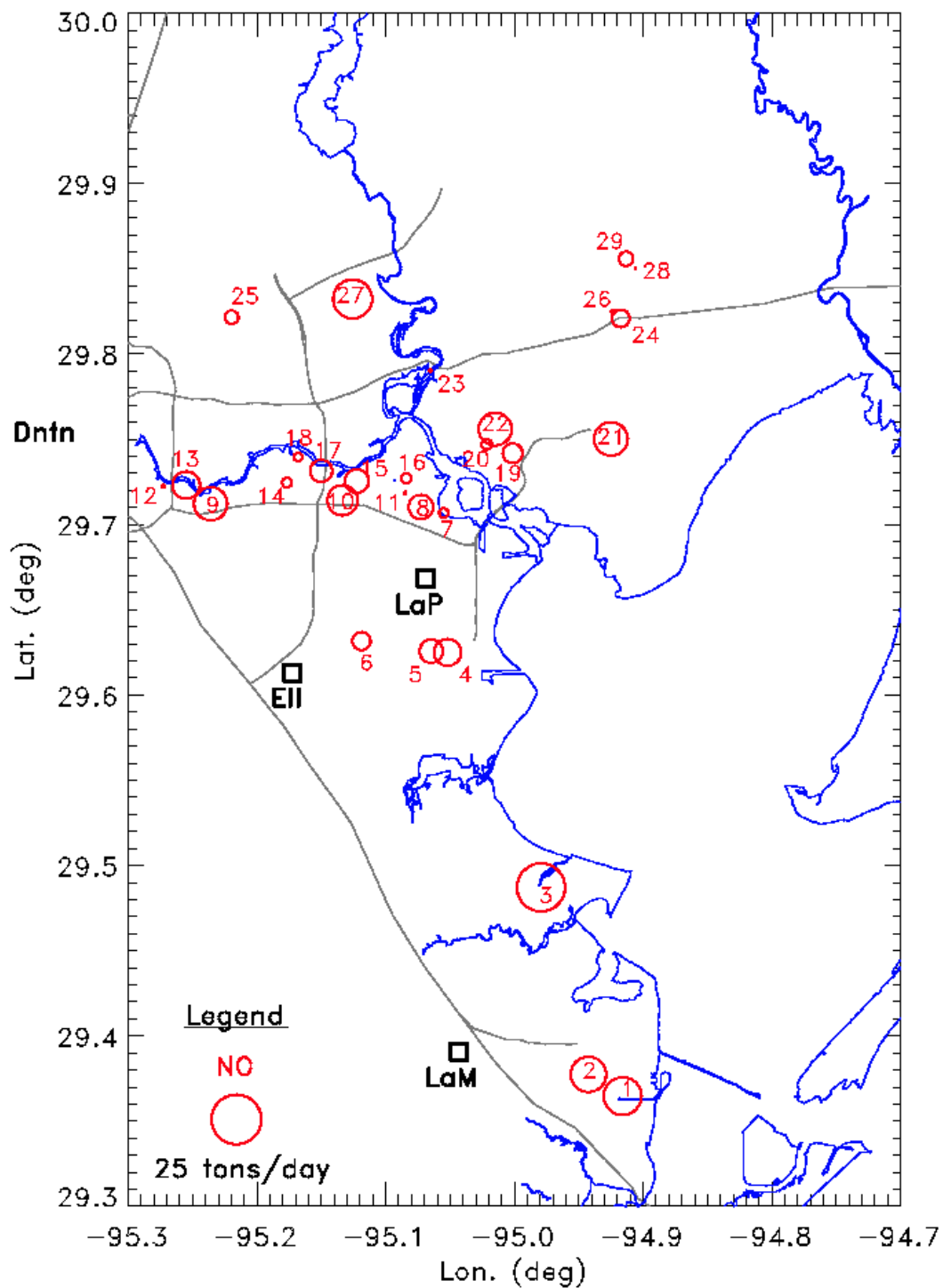
Figure 5. Locations and emission rates of NOx for the 29 "aggregate" major point sources in the Texas City and Ship Channel Complex clusters. Also shown is the identification by a number (1 to 29) of each of these sources. The diagnostic model-data analysis is done for each of these sources, and revised emission rates of NOx and VOC are inferred for each.
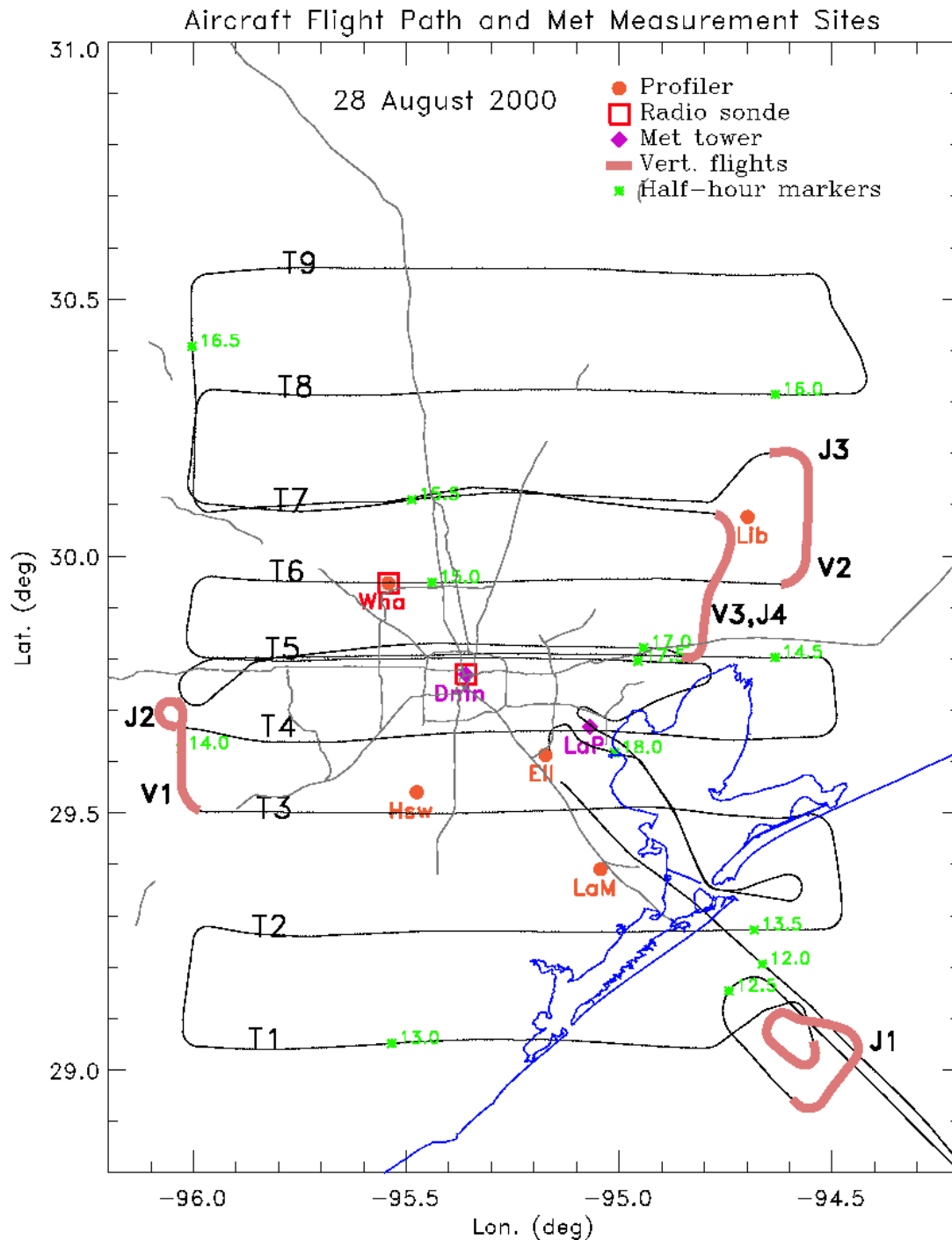
Figure 6. Map of the H-G area showing the NCAR-Electra flight path of 28 Aug 2000, along with the locations of meteorological measurement sites. The colored portions of the aircraft flight path delineate locations of ascent or descent for which the data are used either for vertical soundings of J_{NO2} (J_i, i = 1-4) or variables used to infer Z_i at locations V_i (i = 1-3)

Wind profiler forward trajectories

Start: 06:00 CST 08/28/00
End: 18:00 CST 08/28/00
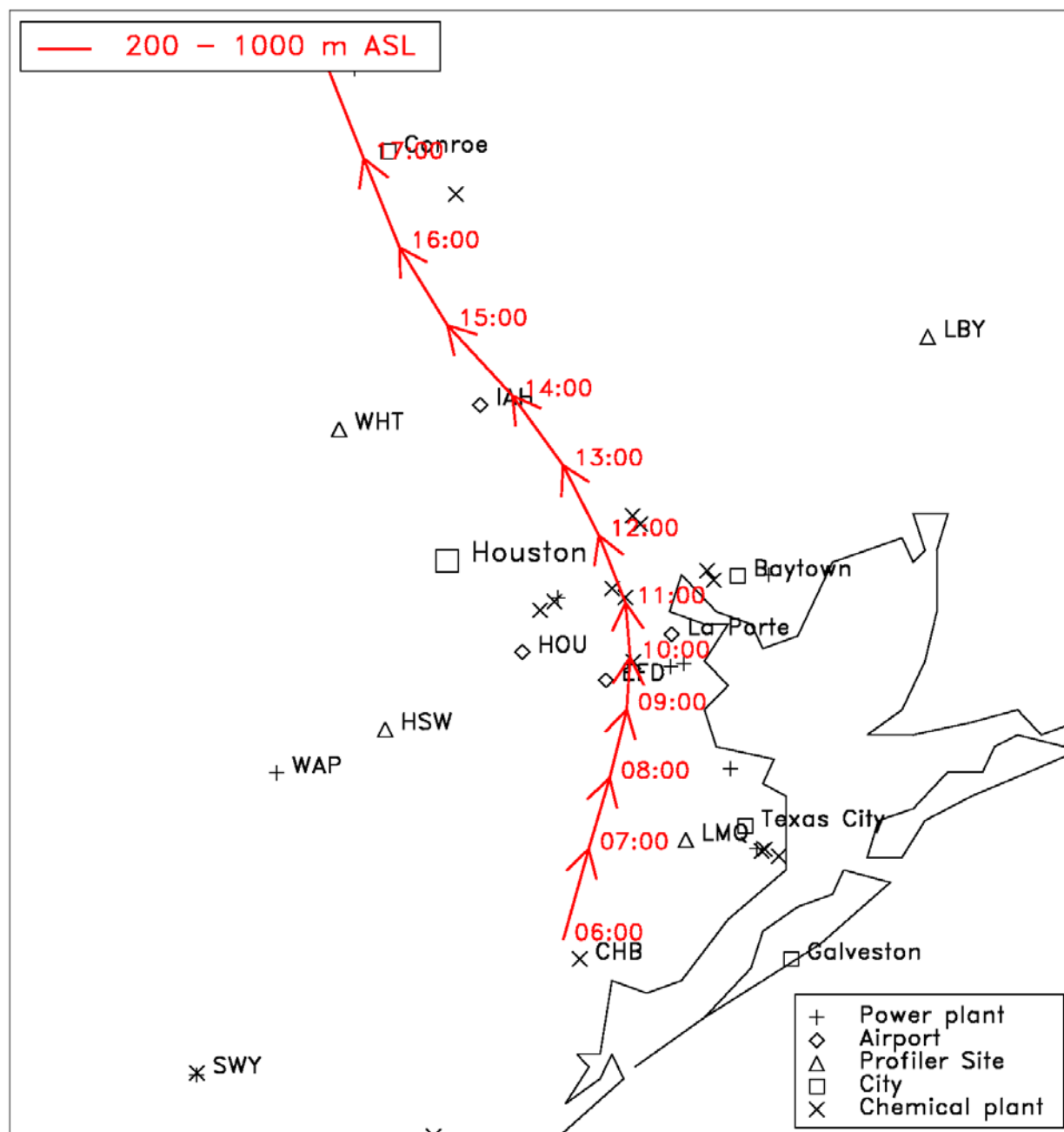
Figure 7. Map of the H-G area showing transport wind trajectory in the layer 200 – 1000 m ASL
for the period 0600 – 1800 CST on 28 Aug 2000, based on profiler winds.
(Plot taken from Senff et al., 2002)
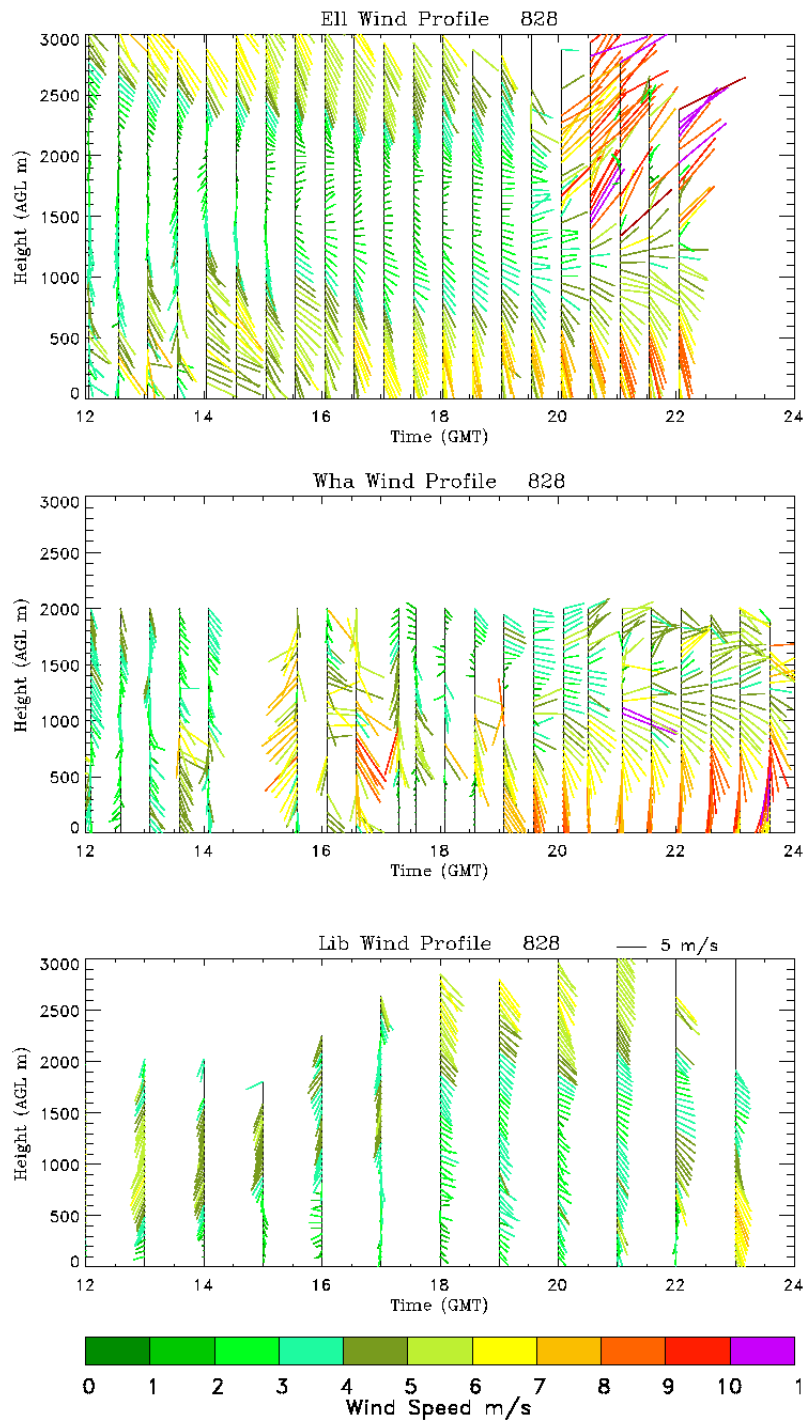
Figure 8. Hourly wind vector vertical profiles based on profiler measurements at three sites: Ellington (Ell), Wharton (Wha) and Liberty (Lib).
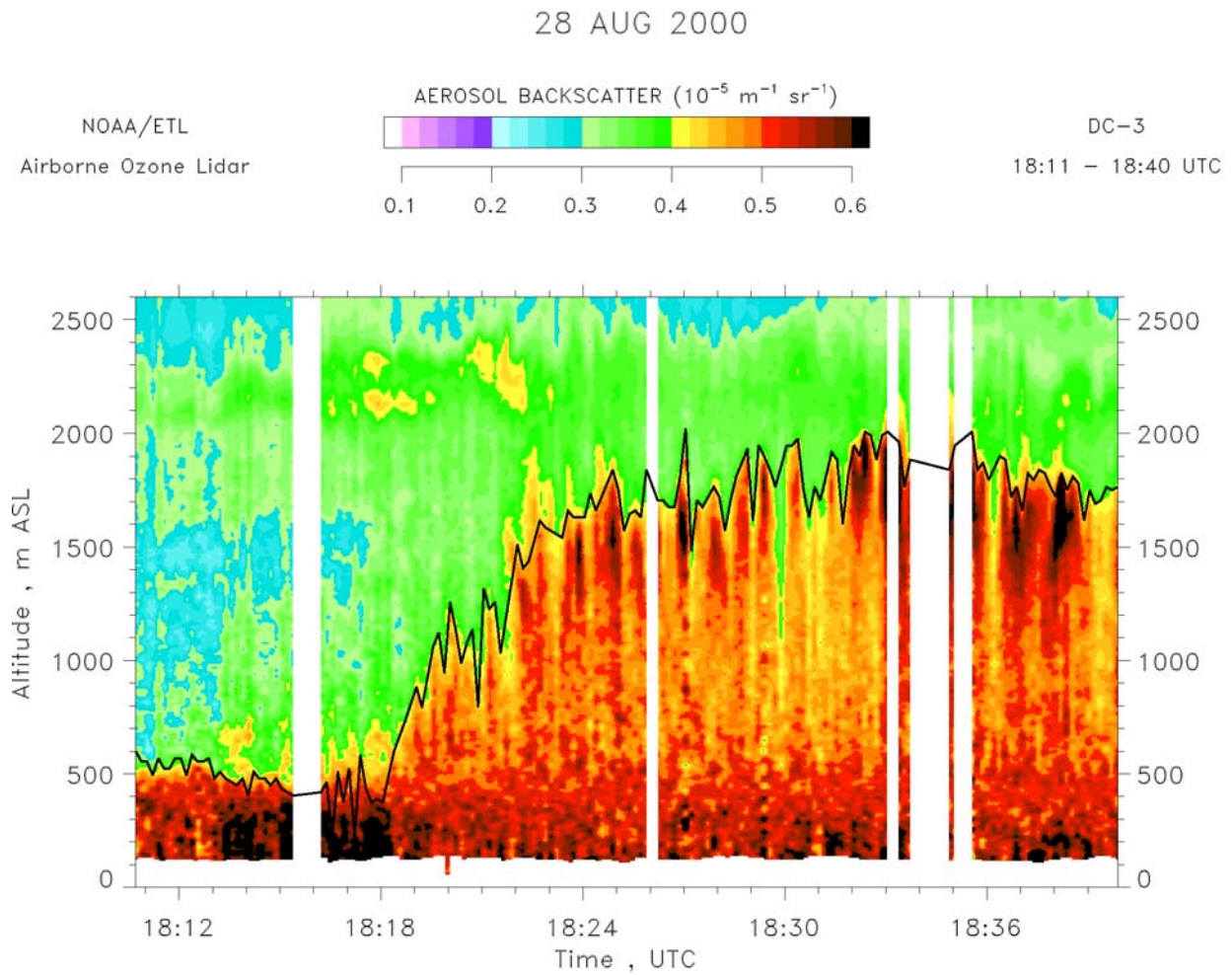
Figure 9. Time-height plot of aerosol backscatter measured with the NOAA-ETL airborne lidar on 28 Aug 2000 (early afternoon). The black line represents the lidar-retrieved mixed layer depth. The plot provides a snapshot of the sharp gradient in mixed layer depth between the Gulf of Mexico (left) and inland (right) --- see Fig. 10 (1210-1240 CST) for aircraft location during the above measurements. (Plot taken from Senff et al., 2002)
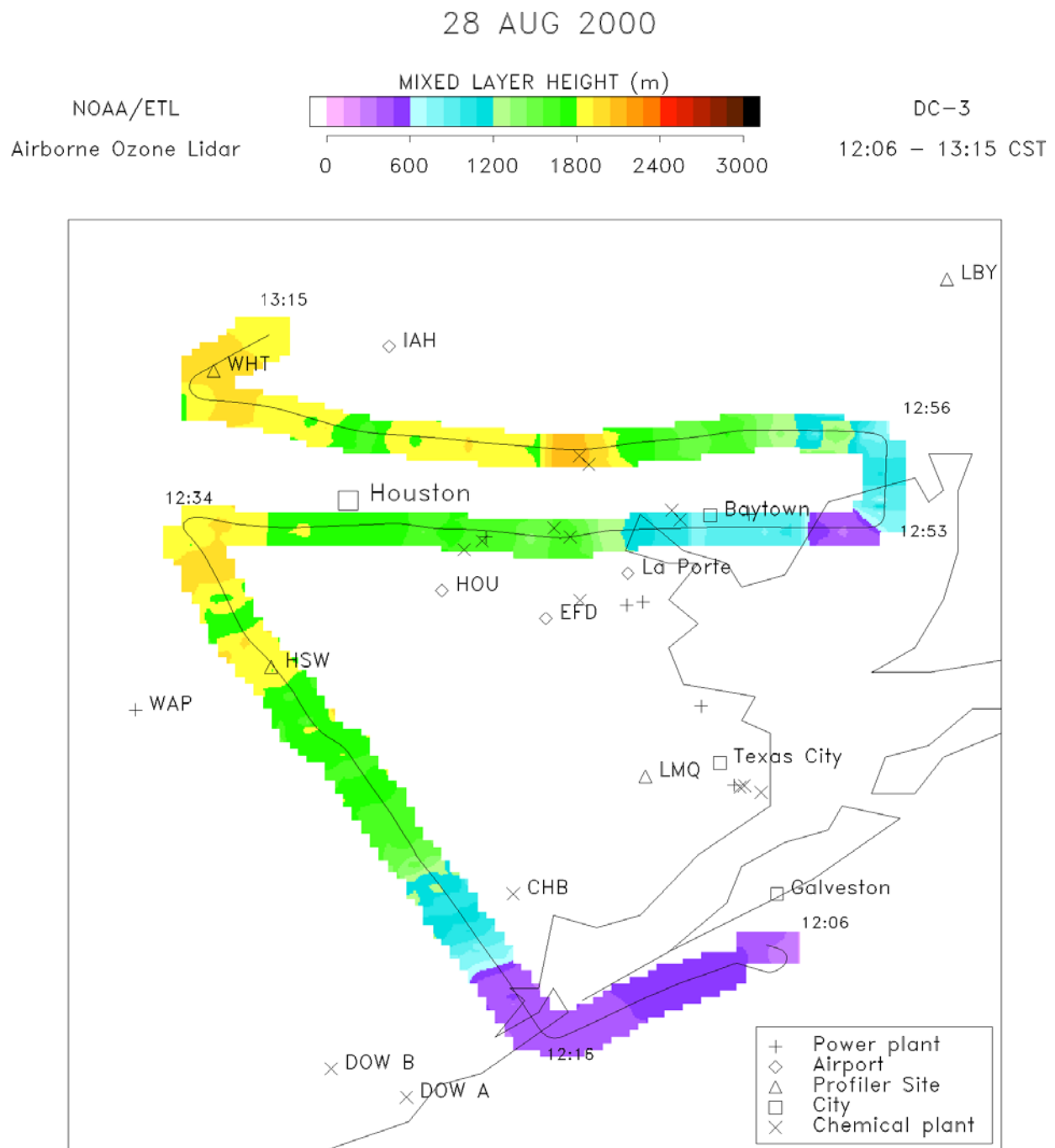
Figure 10. NOAA-ETL lidar aircraft flight path (1206 – 1315 CST) and
corresponding estimated mixed layer height.
(Plot taken from Senff et al., 2002)
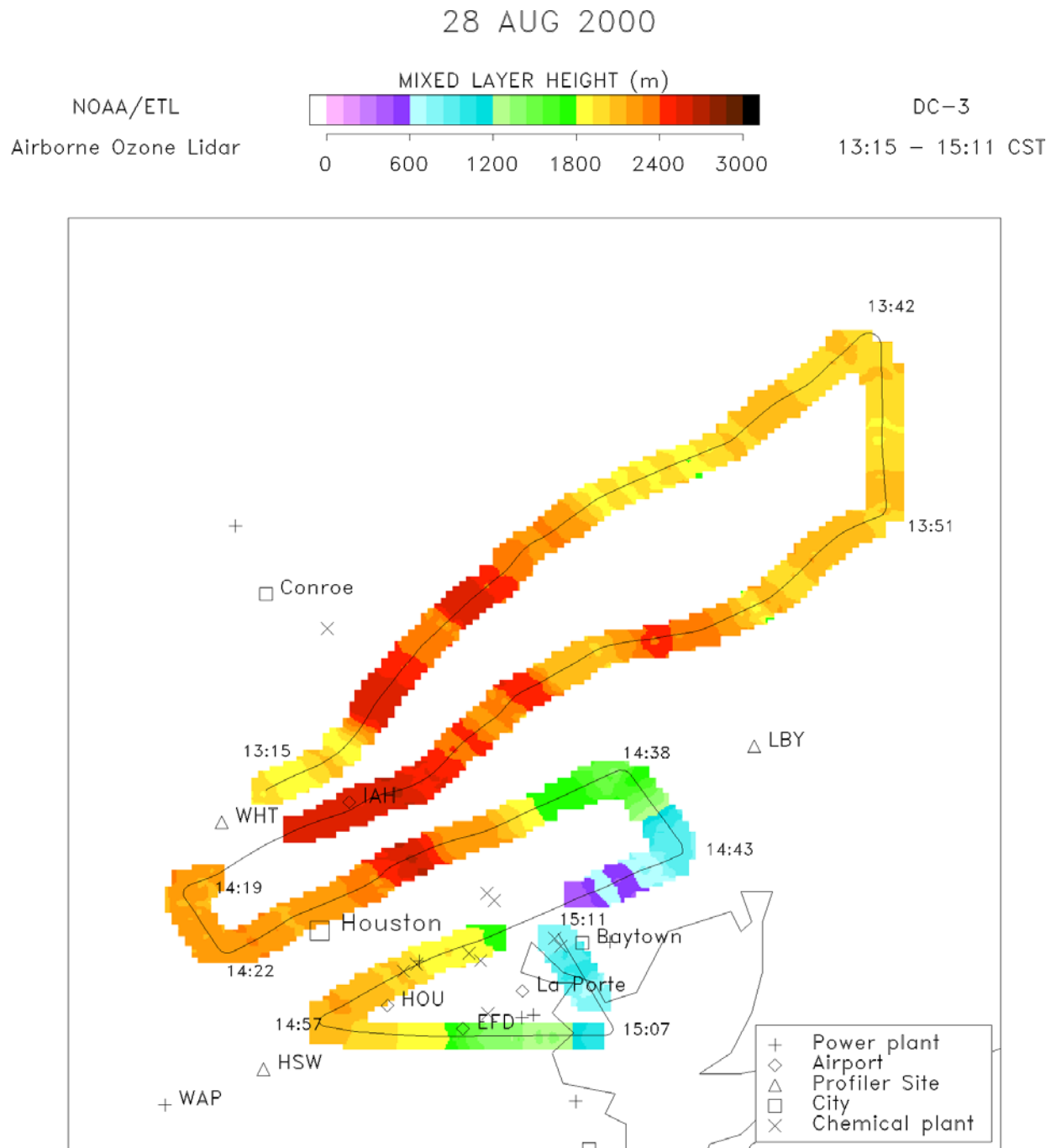
Figure 11. NOAA-ETL lidar aircraft flight path (1315 - 1507 CST) and
corresponding estimated mixed layer height.
(Plot taken from Senff et al., 2002)
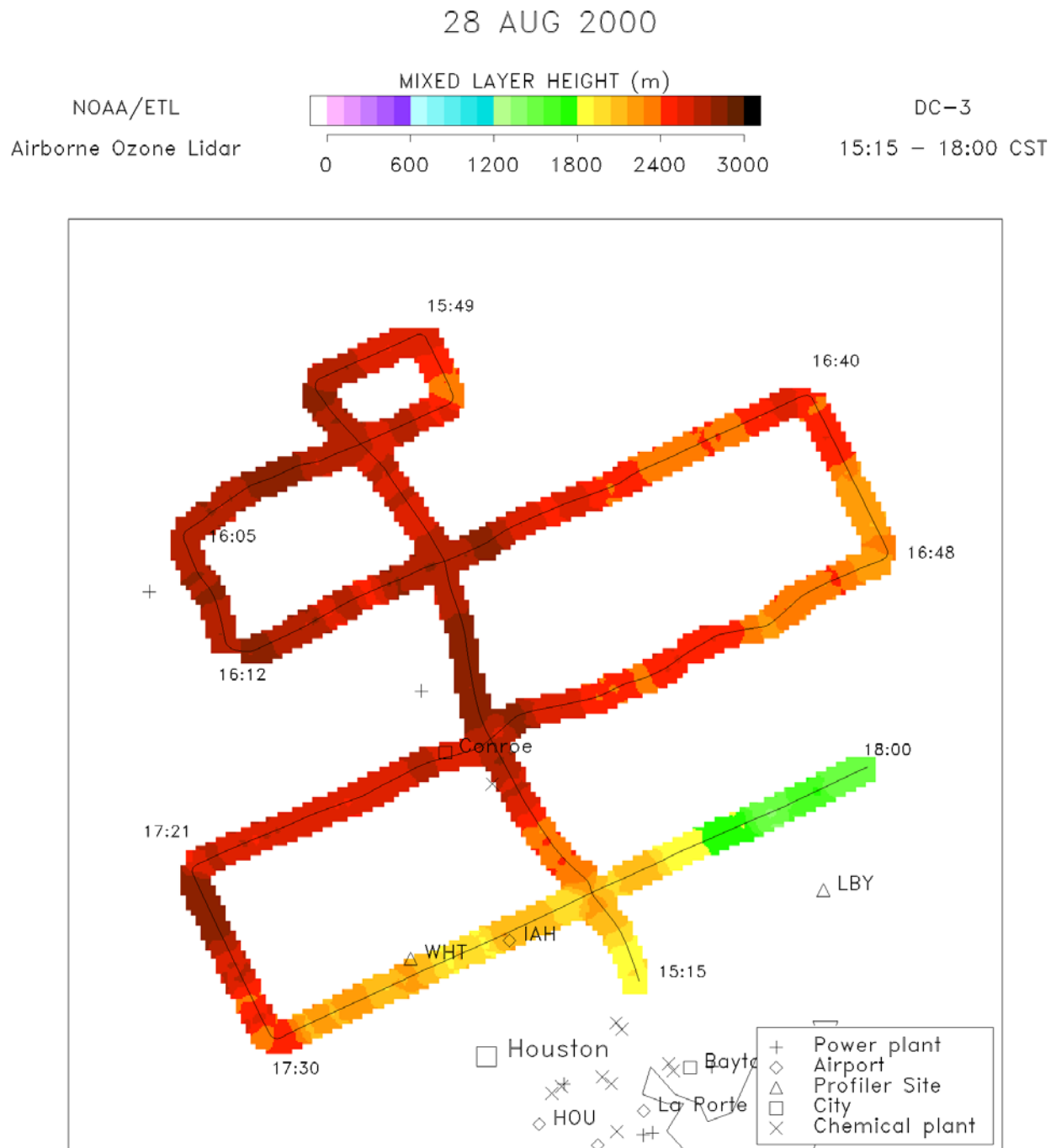
Figure 12. NOAA-ETL lidar aircraft flight path (1515 – 1800 CST) and corresponding estimated mixed layer height. (Plot taken from Senff et al., 2002)
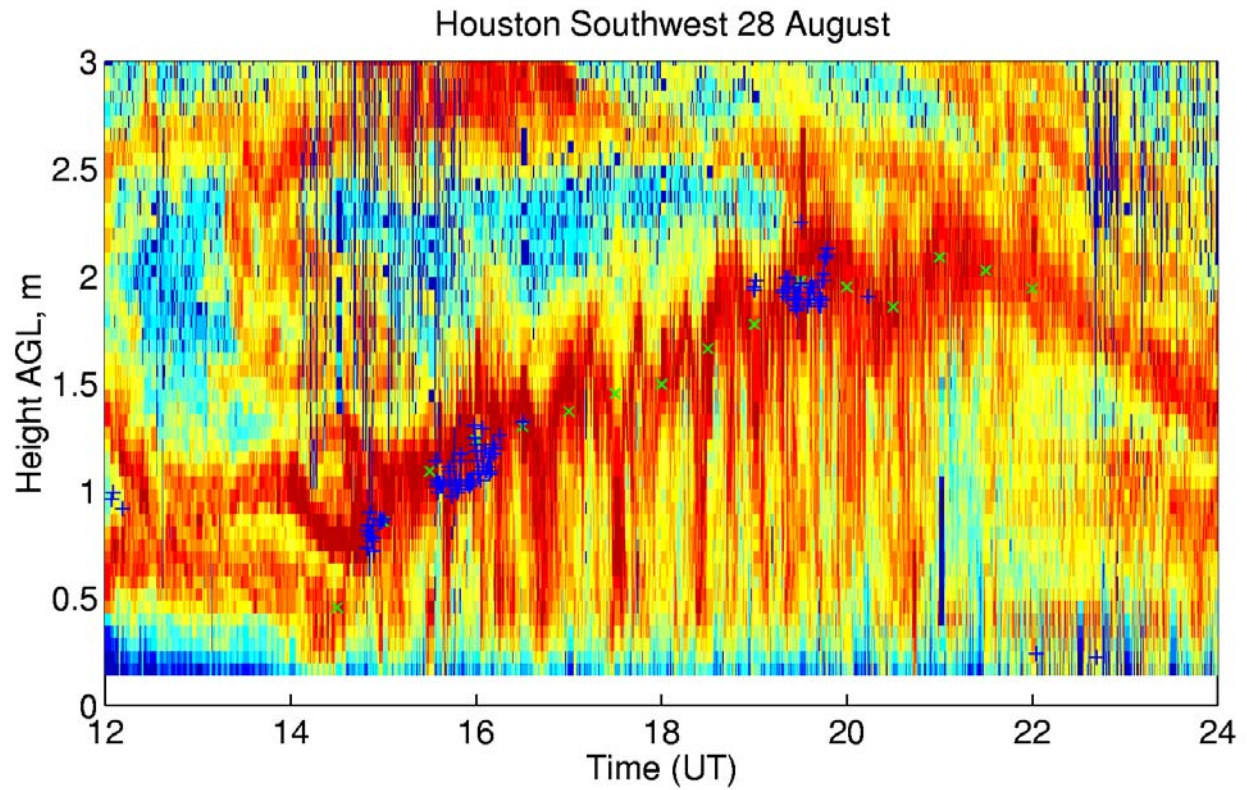
Figure 13. Time-height plot of radar reflectivity measured by Houston Southwest (Hsw) profiler on 28 Aug 2000.
Mixed layer depth estimates are indicated by green "x"s. The crosses denote cloud base height measurements
From a collocated ceilometer. (Plot taken from Senff et al., 2002)
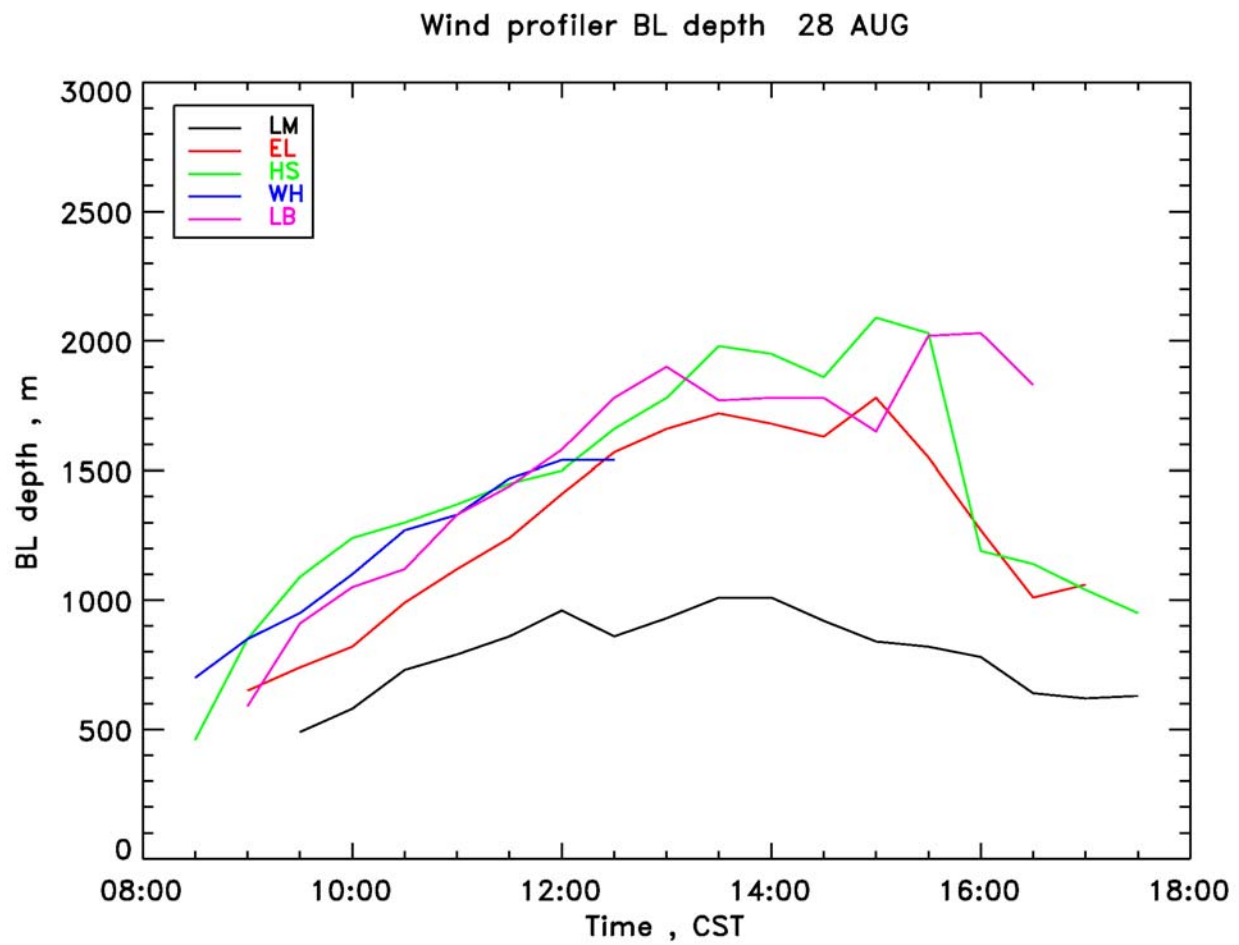
Figure 14. Hourly temporal plot of mixed layer heights inferred from profiler data of radar reflectivity. (LM = LaMarque; EL = Ellington; HS = Houston Southwest; WH = Wharton; LB = Liberty) (Plot taken from Senff et al., 2002)
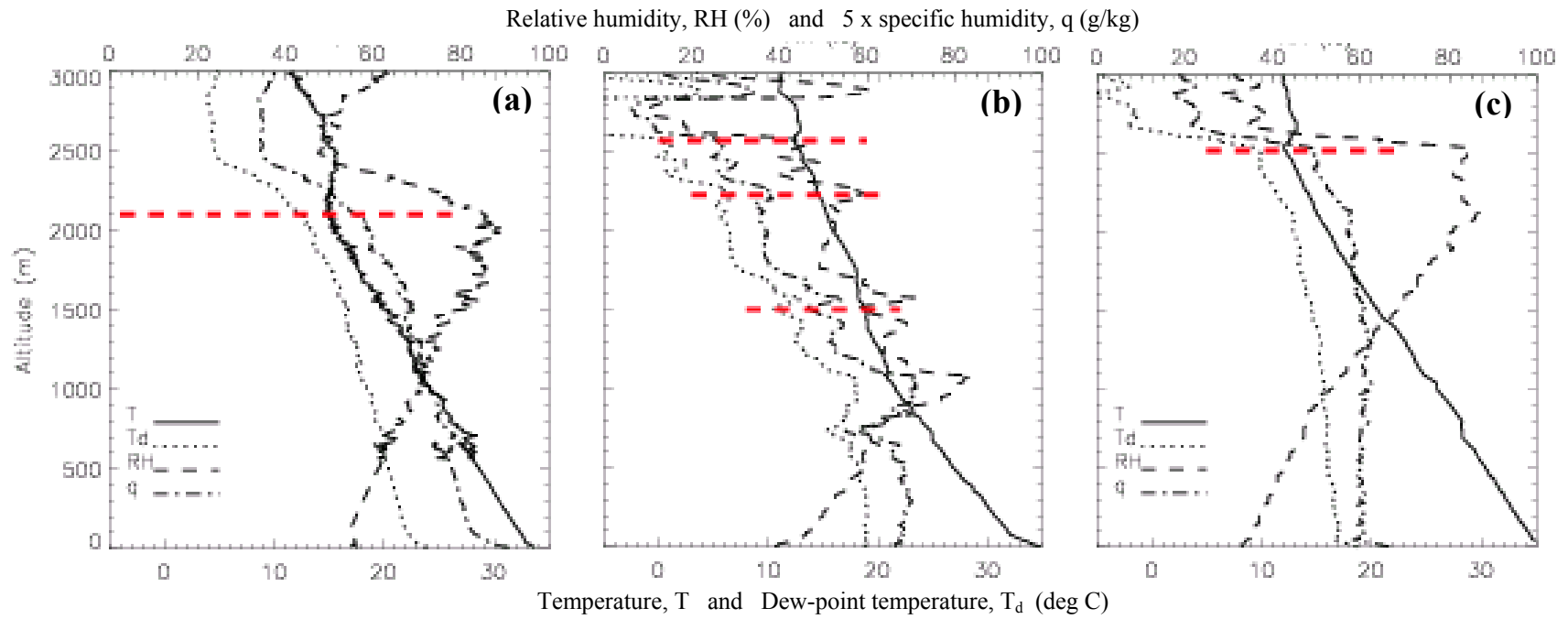
Figure 15. Met soundings for the Downtown (a) and Wharton (b, c) radiosondes at the following times (CDT: (a) 1035 , (b) 1202 , and (c) 1753. The red dashed lines delineate elevated inversion base heights (Z_i).
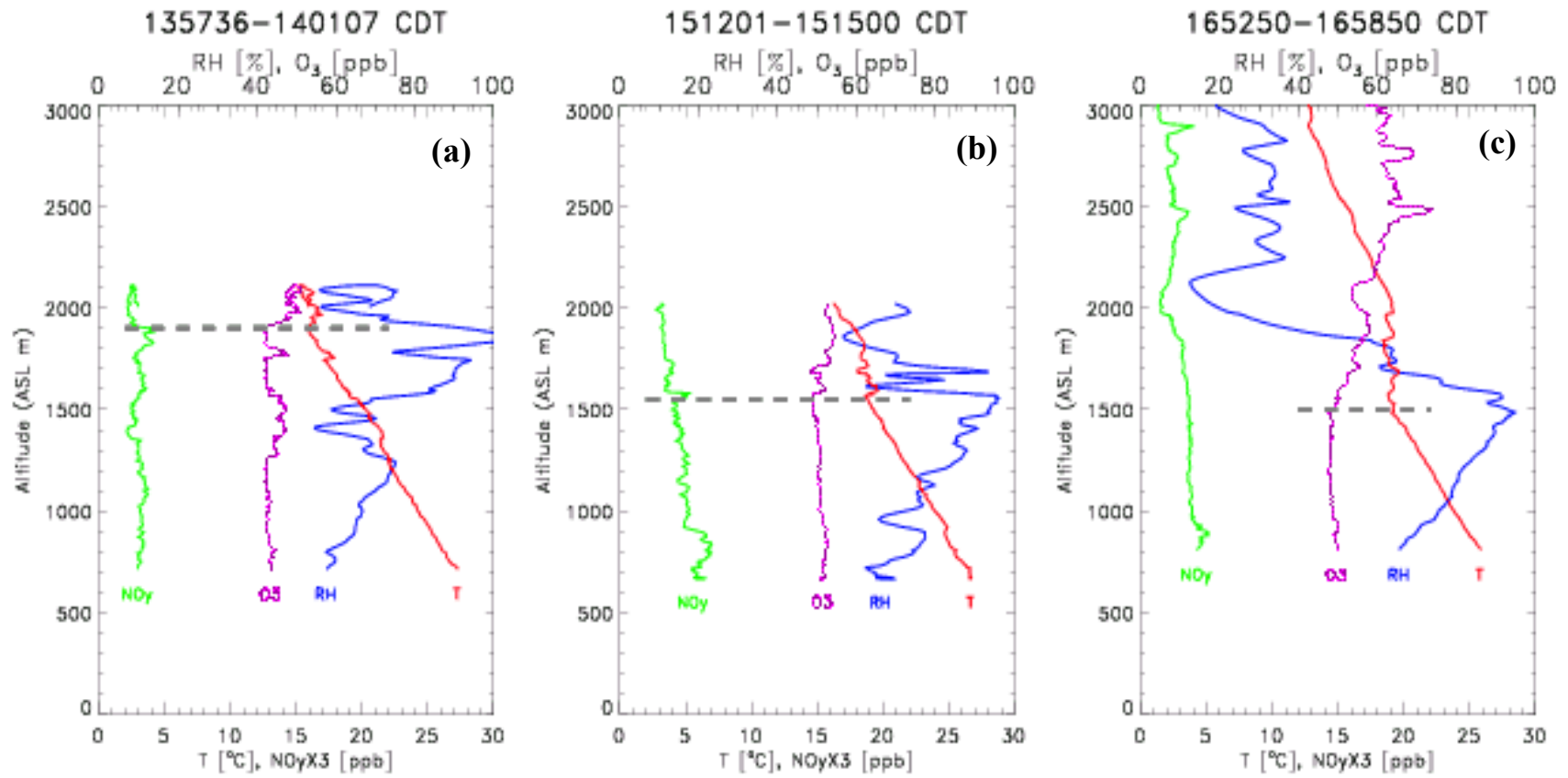
Figure 16. Vertical aircraft sounding results of the variables temperature (T), relative humidity (RH), NO_y and O_3 at locations V_1 (a), V_2 (b) and V_3 (c) shown in Figures 6 and 17.
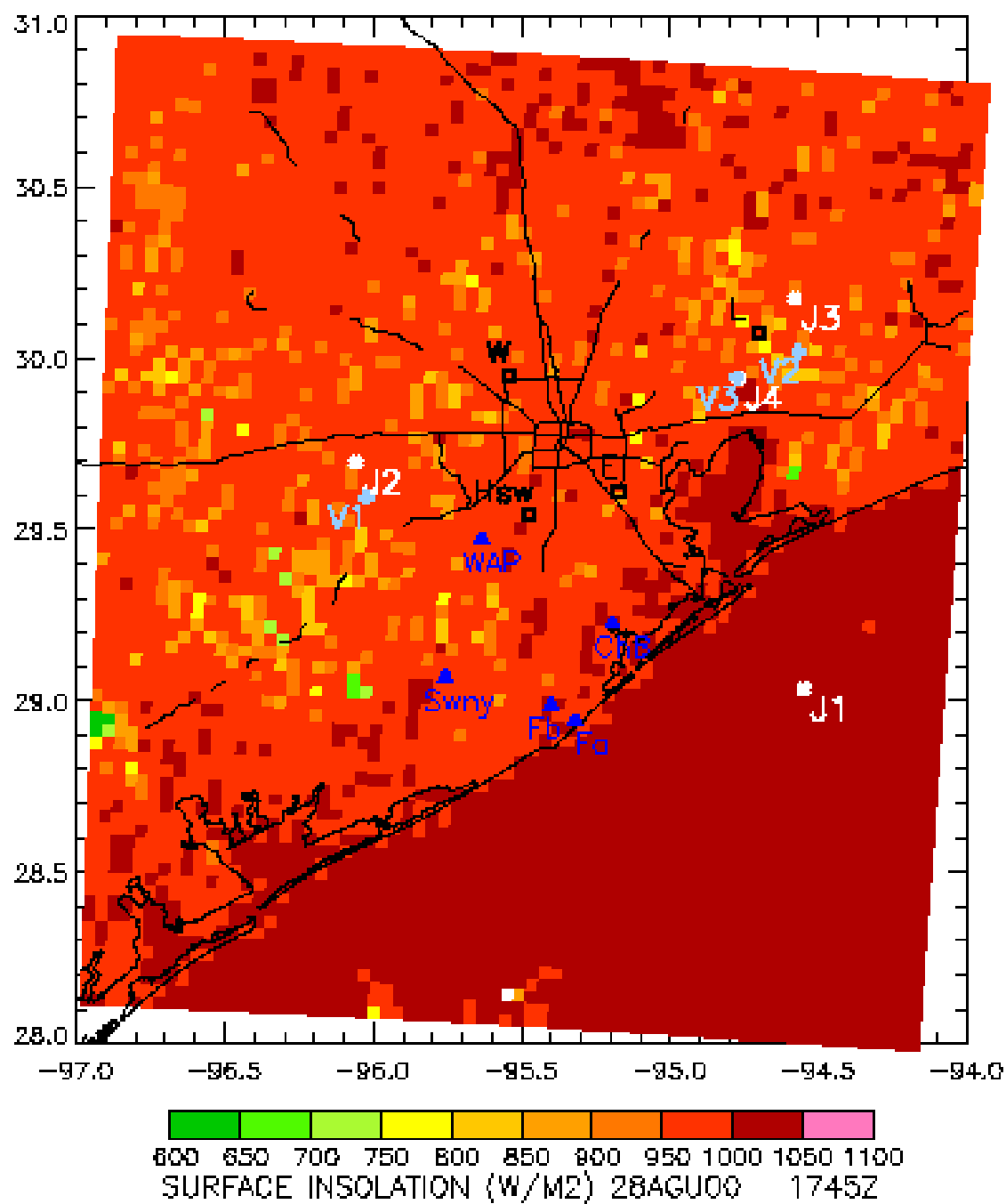
Figure 17. Map of the study area showing satellite (GOES-8)-observed surface insolation. Locations marked J_i (i = 1-4) and V_i (i = 1-3) indicate locations along the Electra flight path which were highlighted in Figure 6 as vertical flight segments
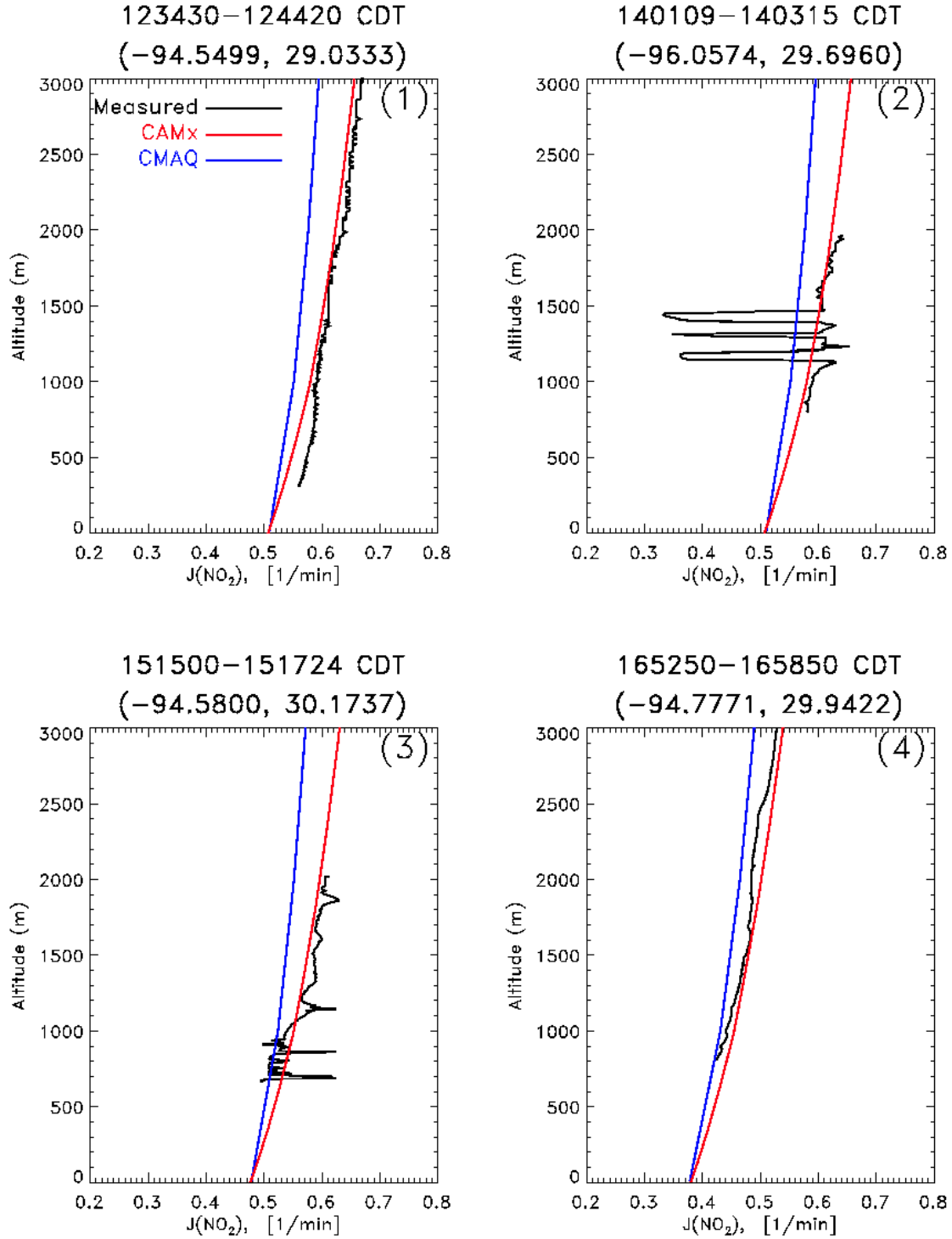
Figure 18. Comparison of J_{NO2} values: the model values (CAMx and CMAQ) are as calculated for the clear sky ; the measured values are from the NCAR Electra measurements. The four panels are for data corresponding to the four locations marked J_i, i = 1, 2, 3, 4 in Figures 6 and 17.
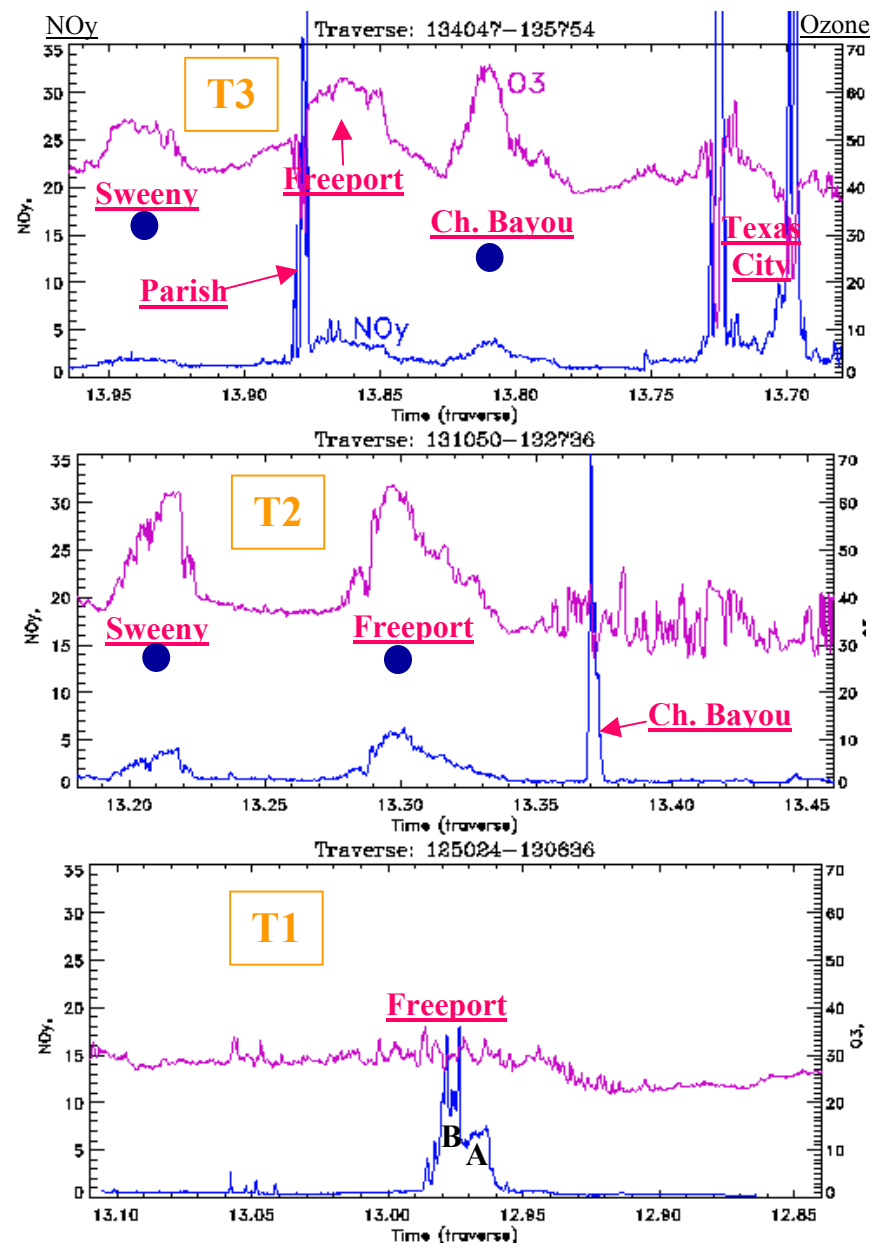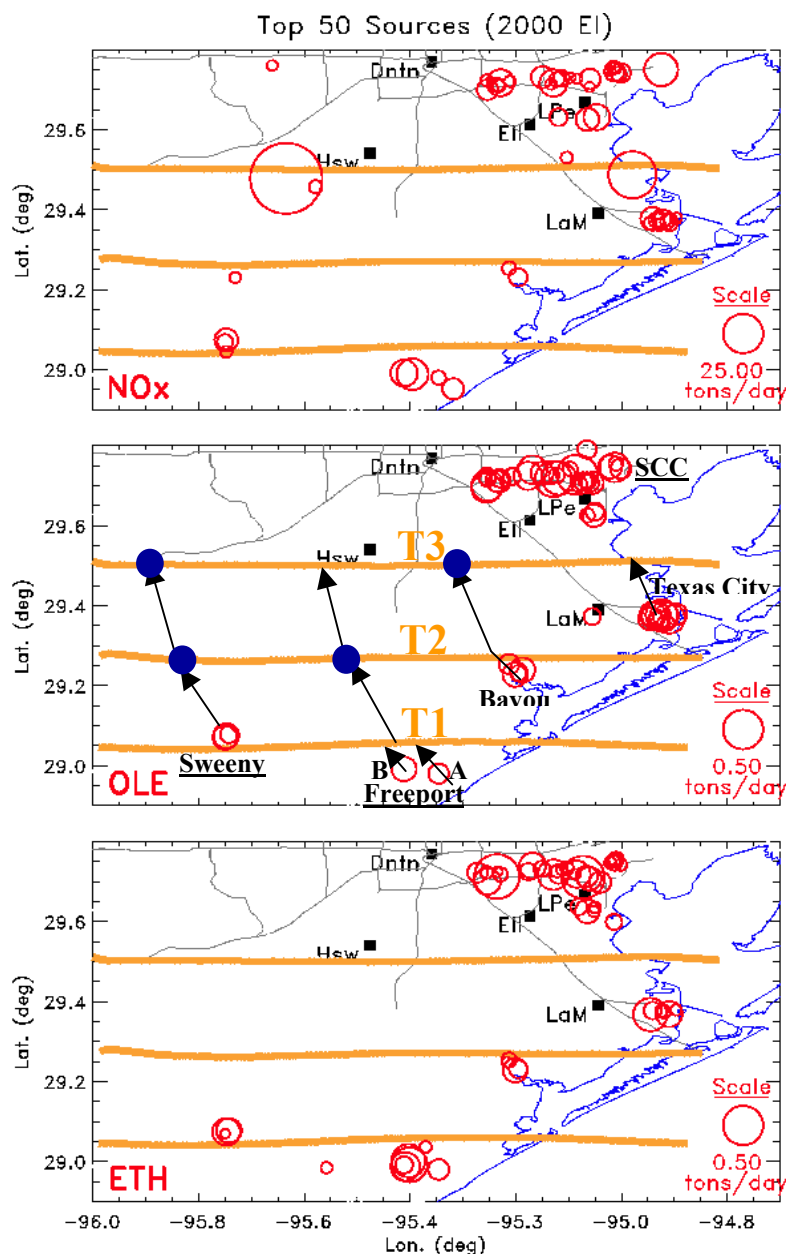
Figure 19. *Left panels*: Locations of the first three (southernmost) traverses (T1, T2, T3) of the NCAR Electra and major point sources of NOx, OLE and ETH, along with the approximate trajectories of the main plumes ; *Right panels*: The Electra data of NOx and O₃ for the three traverses, with the main plumes identified (Parish is the large NOx source, a power plant, in the top left panel, just to the southwest of "Hsw" and just to the south of T3 near its left end).
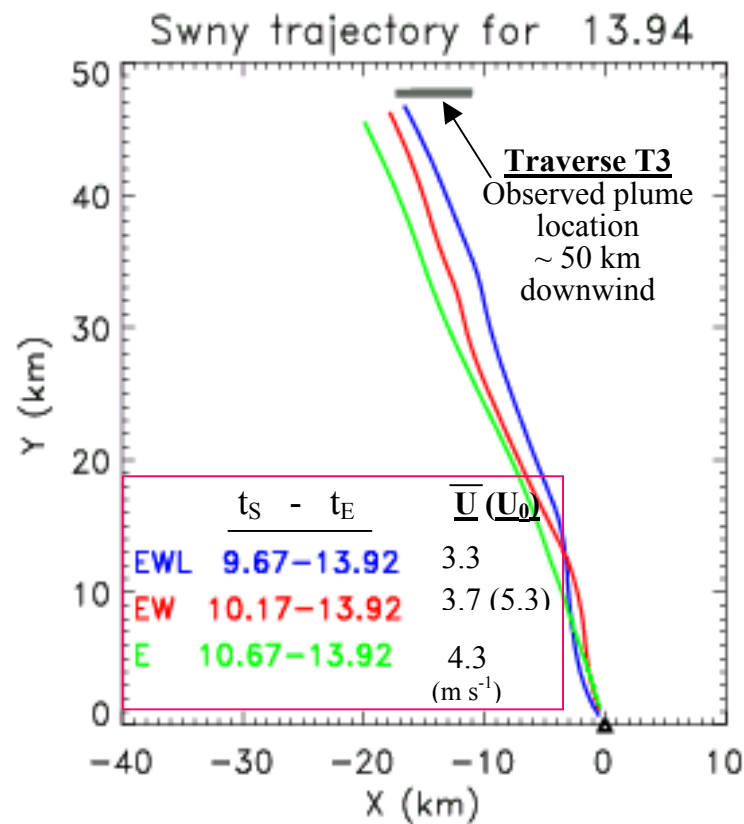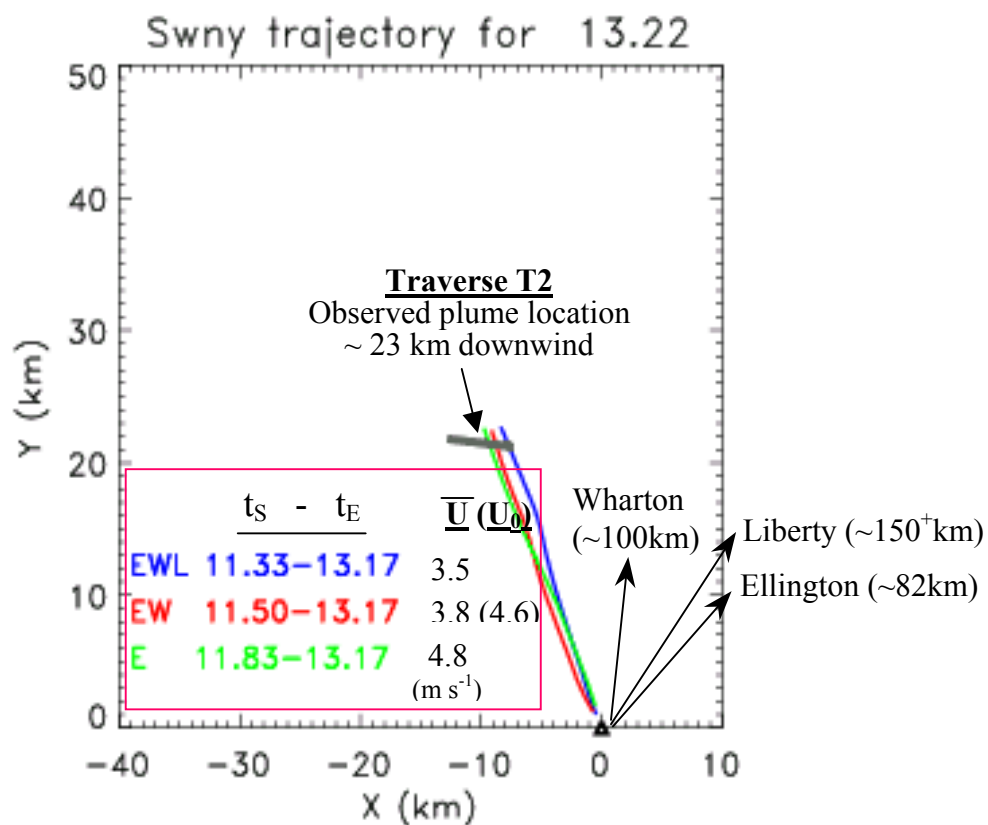
Figure 20. Some pertinent plume dynamics information (observed and simulated) for the Sweeny plumes sampled in the Electra traverses T2 and T3.   The solid triangle denotes the source location; three arrows pointing outwards from there, towards the locations of the three profilers (Ellington [E], Wharton [W] and Liberty [L]) whose wind data were used in calculating plume transport trajectories, are also shown, along with their distances from the source. These trajectories are shown in color : the color coding denotes the particular combination of profiler data used to calculate these trajectories; these combinations (E for Ellington, EW for Ellington and Wharton, and EWL for Ellington, Wharton and Liberty) are also identified, along with the start-end times for each simulated trajectory, for each of which, the average transport speed is also shown (U-bar); the profiler combination EW (red) was selected for the trajectory used in the chemical model simulation (the wind direction was perturbed somewhat to make the trajectory arrive exactly at the observed location of the sampled plume (location shown). The wind speed at effective stack height (U_0), used in the initialization of the plume concentration distribution used in the chemical model, is also shown for the selected profiler combination (EW).
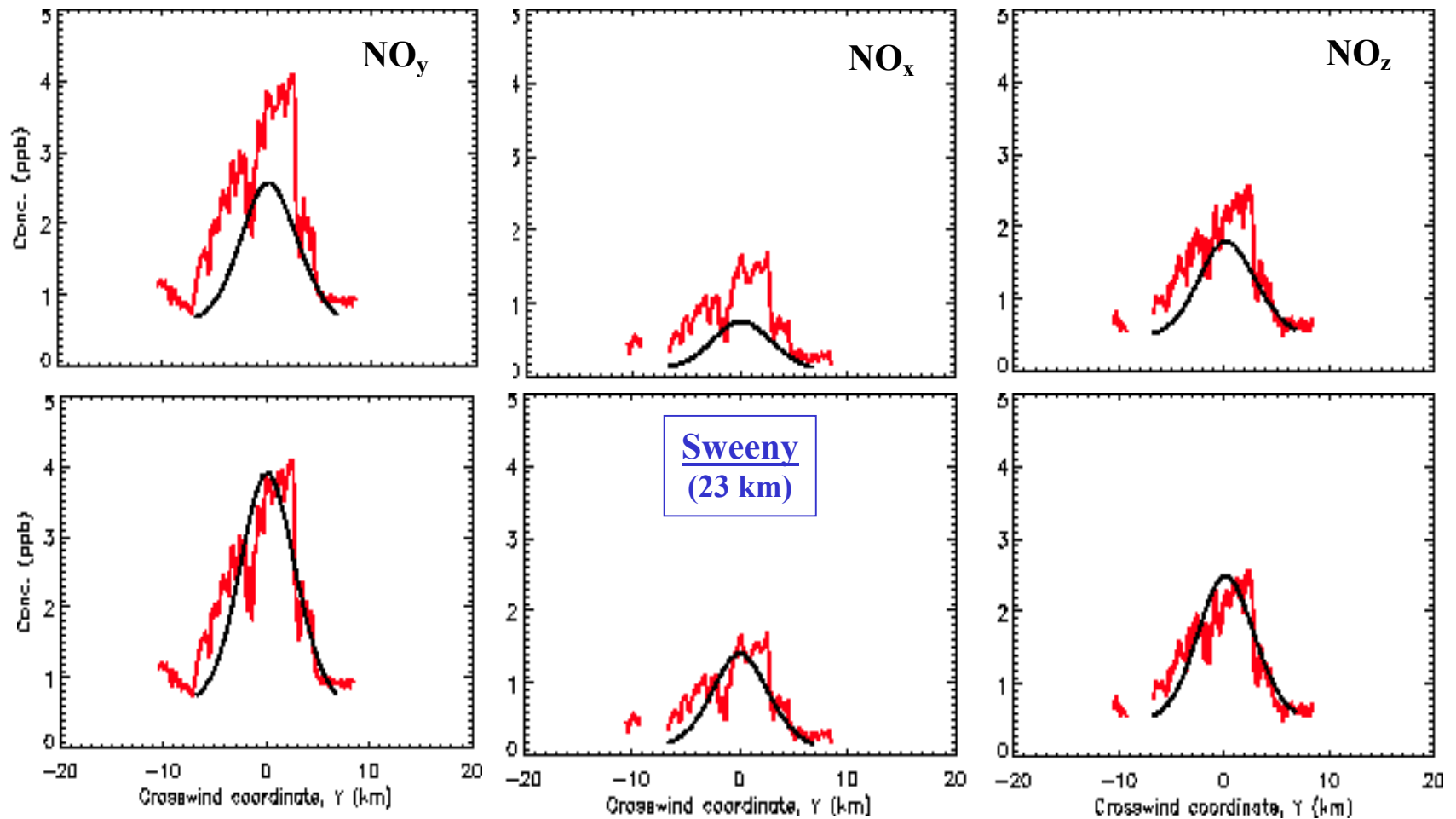
Figure 21. Diagnostic inference of the NOx emission rate, Q_{NOx}, from the composite Sweeny industrial point source : the top panels show a comparison of the measured Electra data (red traces) of NOy, NOx and NOz for traverse T2 of the Sweeny plume and the corresponding LRPM simulated profiles (black traces), using the emission inventory value of Q_{NOx}, i.e., $Q_{NOx}(EI) = 14.5$ Kmol/h; the bottom panels show the same, but using $Q_{NOx} = 1.66$ $Q_{NOx}(EI) = 24.1$ Kmol/h. In both simulations, the winds based on the EW combination are used ($U_0 = 4.6$ m/s, and the average transport wind of 3.8 m/s) and the mixing height variation shown in Fig. 13 is used. Our conclusion is that the lower panels provide a better fit of the measured data, hence, $Q_{NOx} \sim 1.66$ $Q_{NOx}(EI)$ is the inferred NOx emission rate.
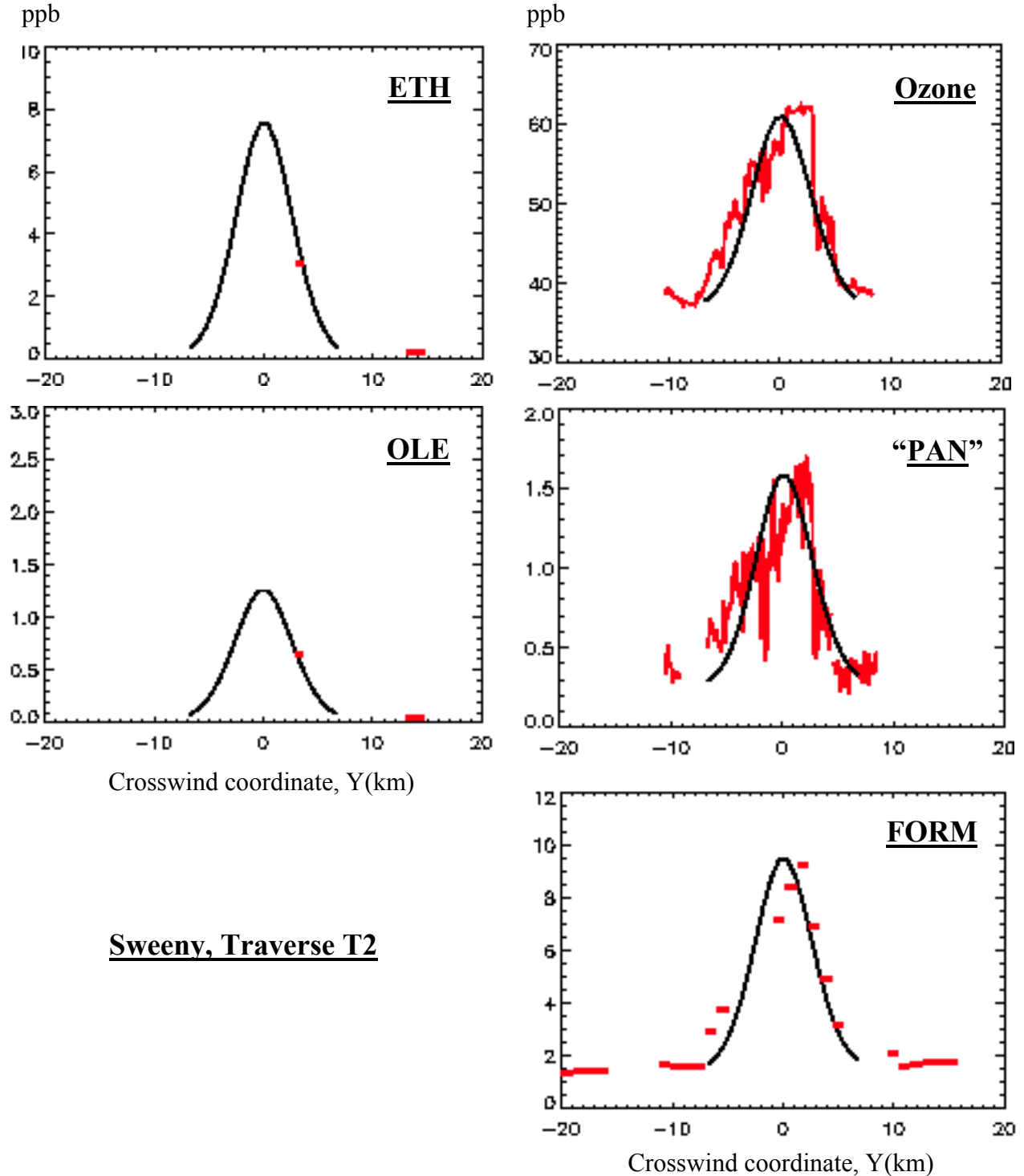
Figure 22. Diagnostic inference of the emission rates of ETH and OLE for the composite Sweeny industrial point source based on the Electra measured data (in red) of traverse T2 (23 km and 1.7h downwind of Sweeny): the good matches shown for ETH, OLE, Ozone, "PAN" = NOz – HNO3, and HCHO correspond to LRPM simulation using $Q_{NOx} = 1.66 \, Q_{NOx}$ (EI), $Q_{ETH} = 3.6 \, Q_{NOx}$ and $Q_{OLE} = 2.0 \, Q_{NOx}$. These inferred estimates of the emission rates of ETH and OLE are two orders of magnitude greater than the corresponding EI values. Using the latter, the simulated values of all five variables shown here were grossly under-estimated.

Sweeny, Traverse T3
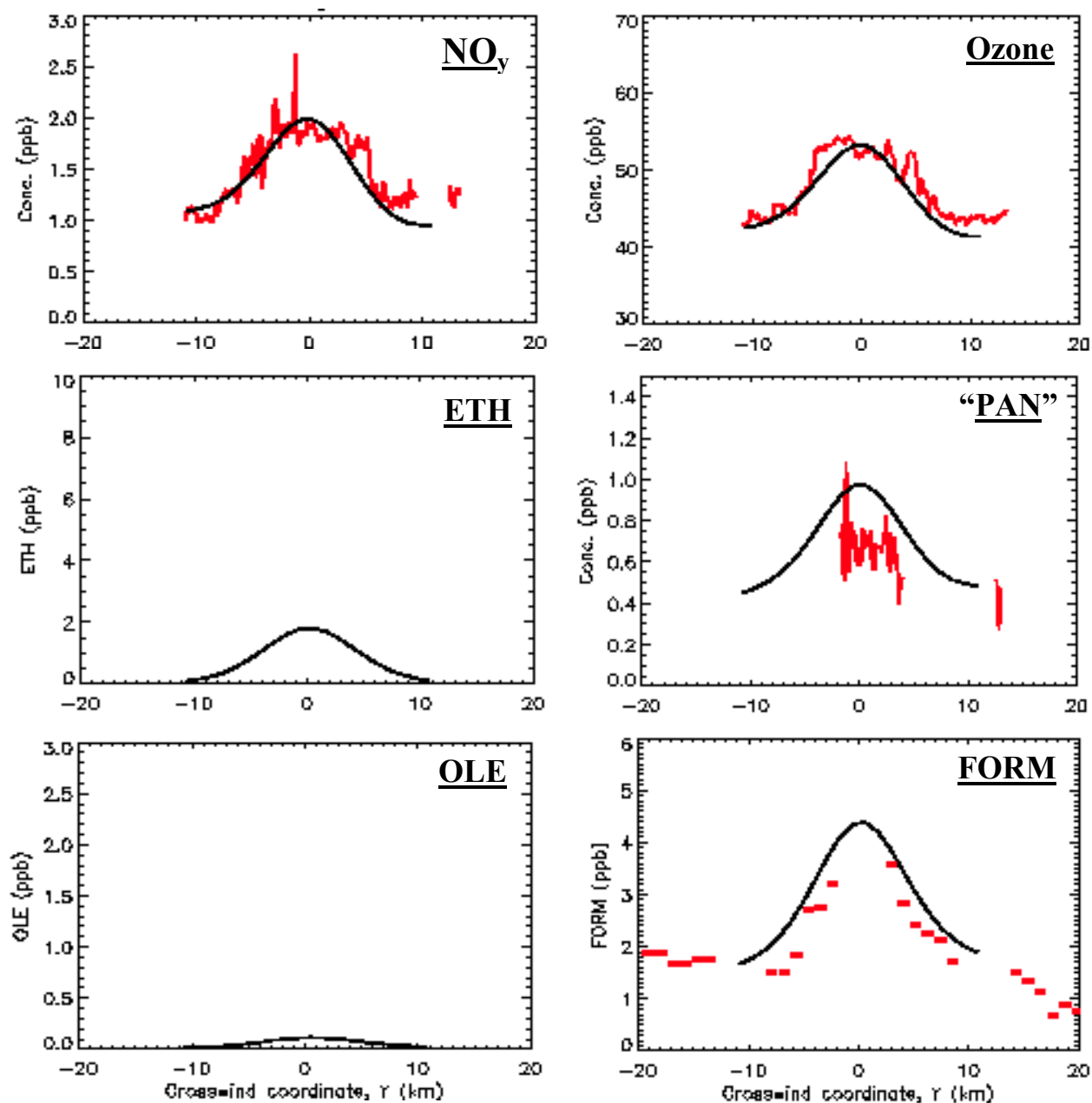

Figure 23. Same as in Fig. 22, except the results here are for the Sweeny plume at Electra traverse T3 (~50 km and 3.75h downwind of the Sweeny source). In this case, the diagnostic inference is based on LRPM simulation of the plume released at about 1010, and using the EW winds, with $U_0 = 5.3$ m/s, the average transport speed of 3.7 m/s, and $Q_{NOx} = 1.25\ Q_{NOx}(EI)$, $Q_{ETH} = 3.6\ Q_{NOx}$ and $Q_{OLE} = 2.0\ Q_{NOx}$, There were no measured data for ETH and OLE in this traverse, and there are also some missing measured data for PAN and HCHO.

The Freeport plumes at Traverse T2
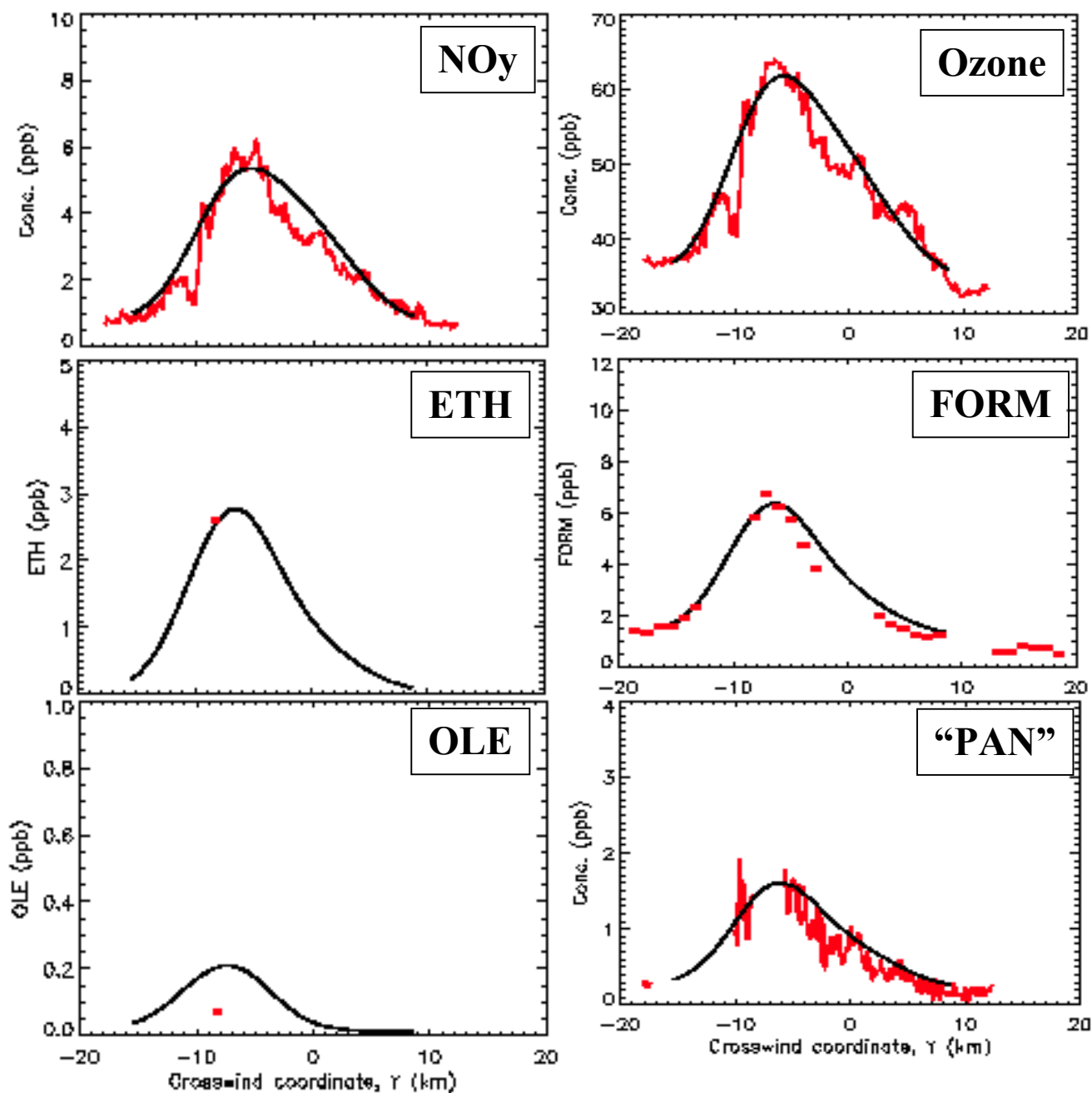
Figure 24. Same as in Fig. 22, except the results here are for the composite Freeport plume (from sources at Freeport A and B, and a source in the middle which we call M) at Electra traverse T2 (~33 km downwind of the composite source). In this case, the diagnostic inference is based on LRPM simulation of the composite plume, using the EW winds, Houston SW profiler Z_i, and the following emission rates:

For Freeport A and M: $Q_{NOx} = 2\ Q_{NOx}(EI)$, $Q_{ETH} = Q_{NOx}$ and $Q_{OLE} = 0.2\ Q_{NOx}$;

For Freeport B : $Q_{NOx} = 1.5\ Q_{NOx}(EI)$, $Q_{ETH} = 1.5\ Q_{NOx}$ and $Q_{OLE} = Q_{NOx}$.

The Chocolate Bayou plume at Traverse T3
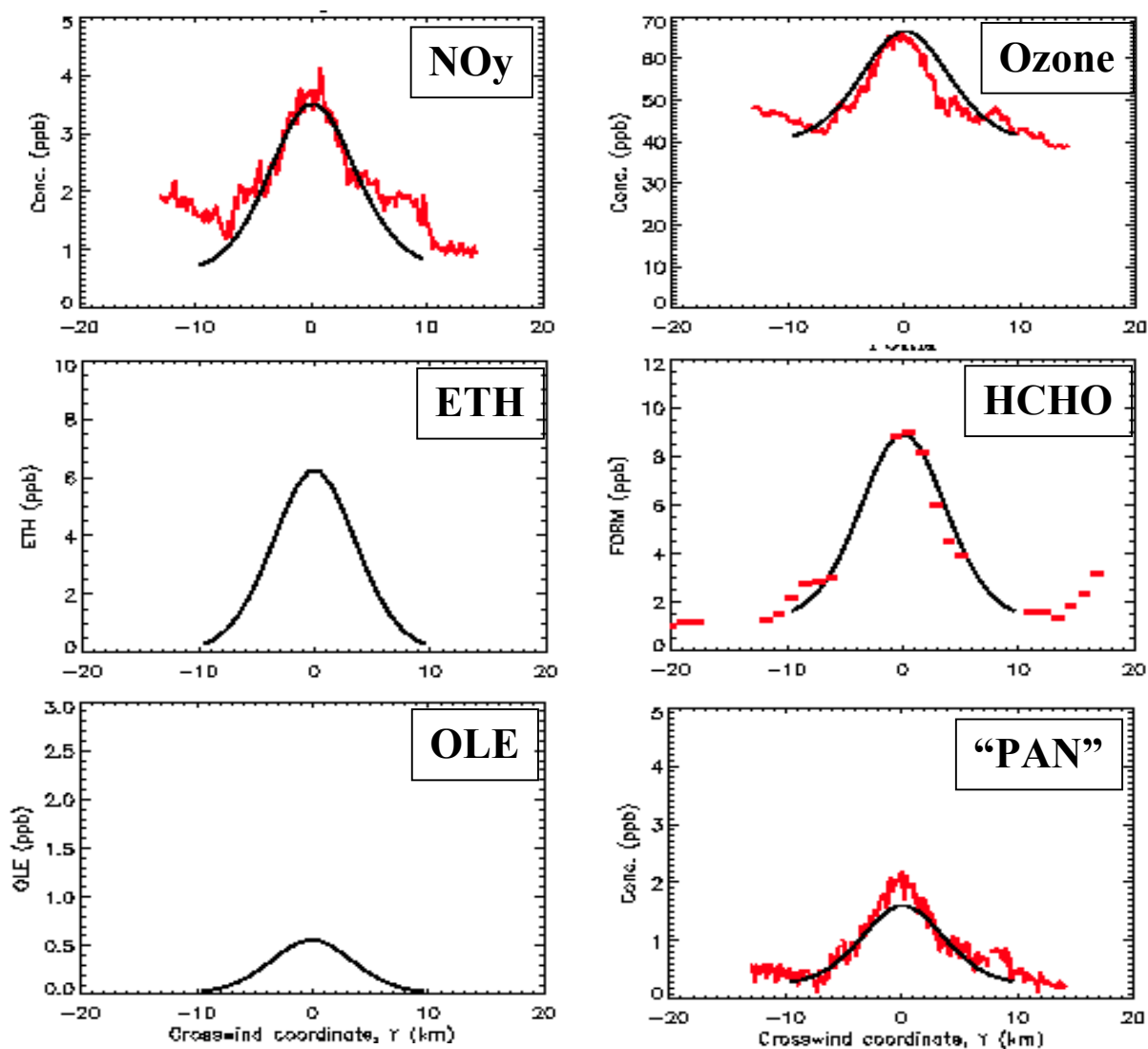
Figure 25. Same as in Fig. 22, except the results here are for the composite Chocolate Bayou plume, at Electra traverse T3 (~33 km downwind of the source). In this case, the diagnostic inference is based on LRPM simulation of the plume using the EW winds, Houston SW profiler Z_i, and $Q_{NOx} = 4.5 \, Q_{NOx}(EI)$, $Q_{ETH} = 4.0 \, Q_{NOx}$ and $Q_{OLE} = 2.0 \, Q_{NOx}$, There were no measured data for ETH and OLE in this traverse.
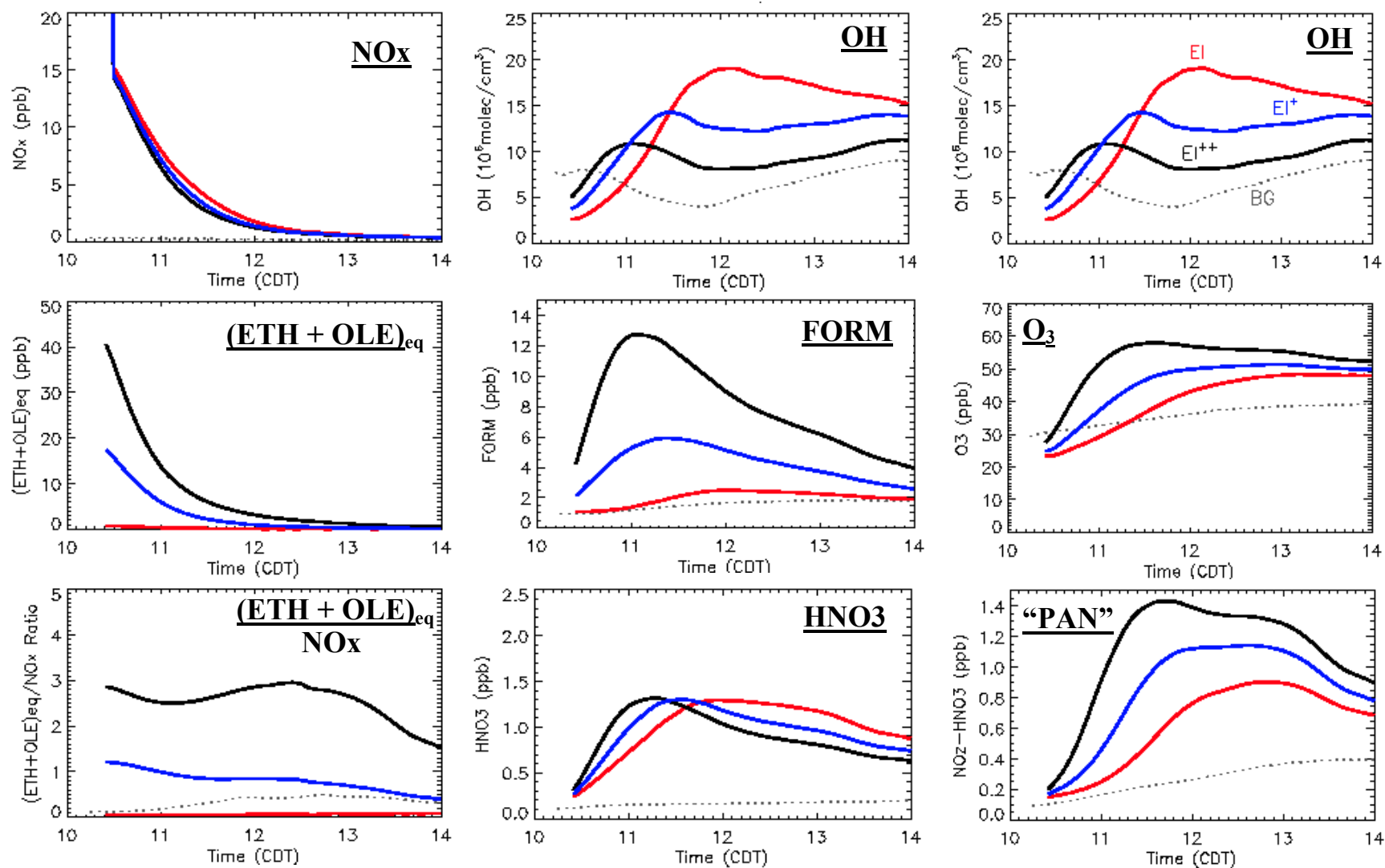
Figure 26. Sensitivity of secondary formations (OH, O_3, HNO$_3$, "PAN" and FORM) to three cases of ETH and OLE emissions from Sweeny for the traverse T3 scenario [plume release at 1010, EW winds, Houston SW Z_i, and $Q_{NOx} = 1.25\ Q_{NOx}(EI)$]. The three cases of ETH and OLE emissions are as follows:-
(Red = EI) : Q_{ETH} and Q_{OLE} as per their emissions inventory ; (Blue = EI+) : $Q_{ETH} = Q_{NOx} = Q_{OLE}$; (Black = EI++) : $Q_{ETH} = 3.6\ Q_{NOx}$ and $Q_{OLE} = 2\ Q_{NOx}$.

Model-data comaparison for Traverse T5, based on emission rates of NOx, ETH and OLE as in the EI
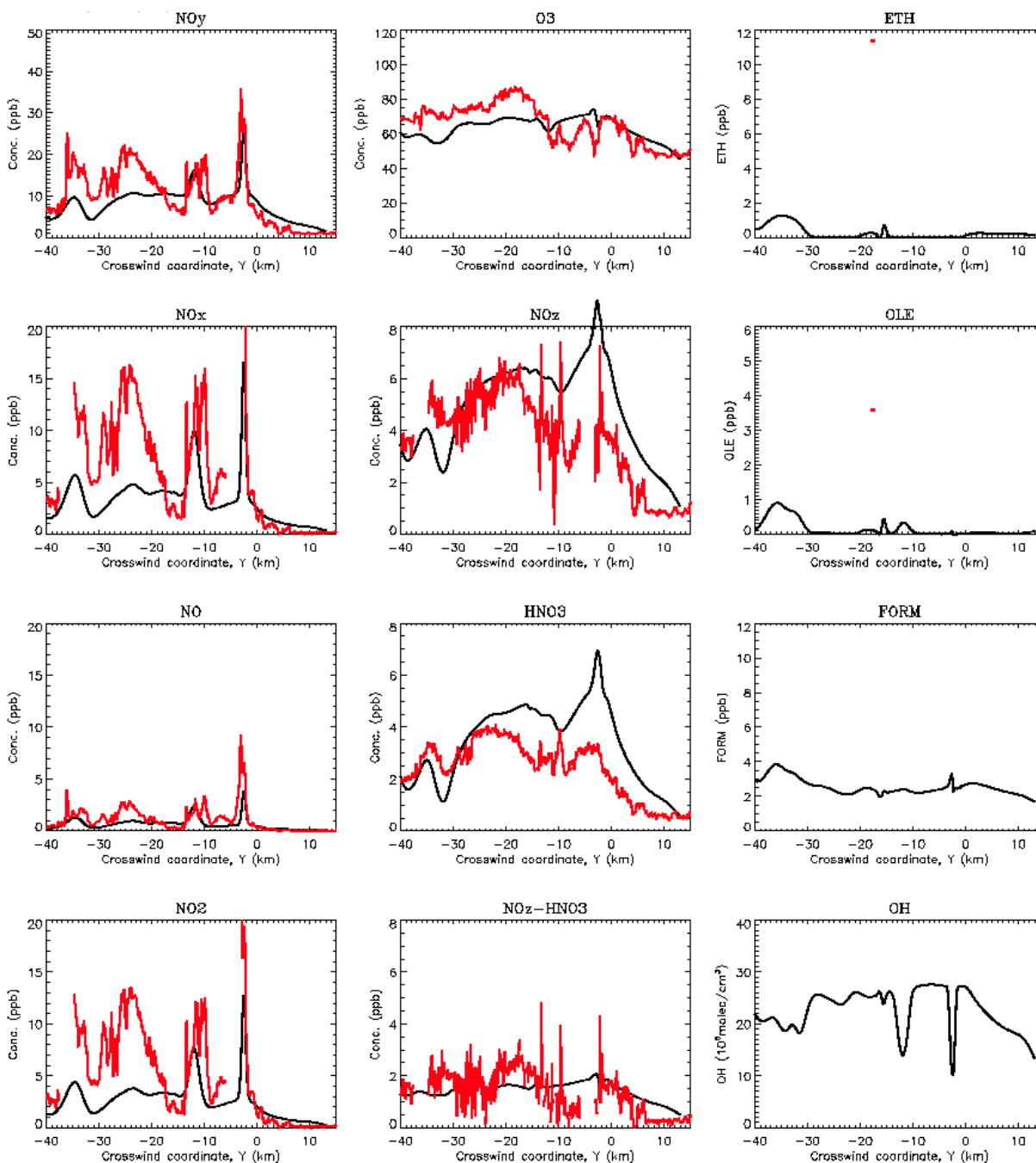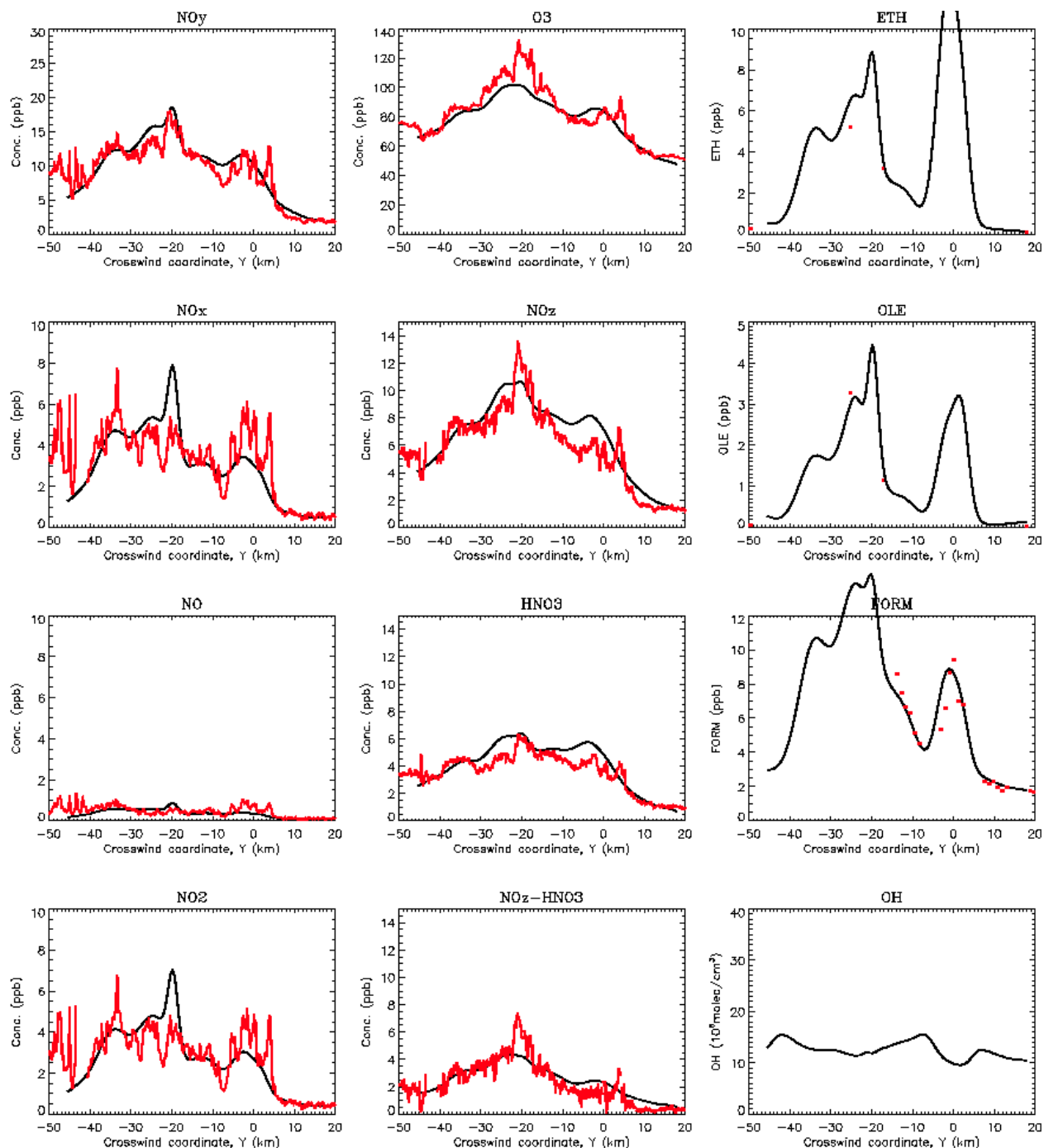

Figure 27. Comparison of measured (in red) and simulated (black) concentration profiles of primary and secondary species for traverse T5 (the first traverse, about 10 km, downwind of the ship channel complex). The simulation is based on NOx and VOC emission rates as in the emissions inventory (EI).

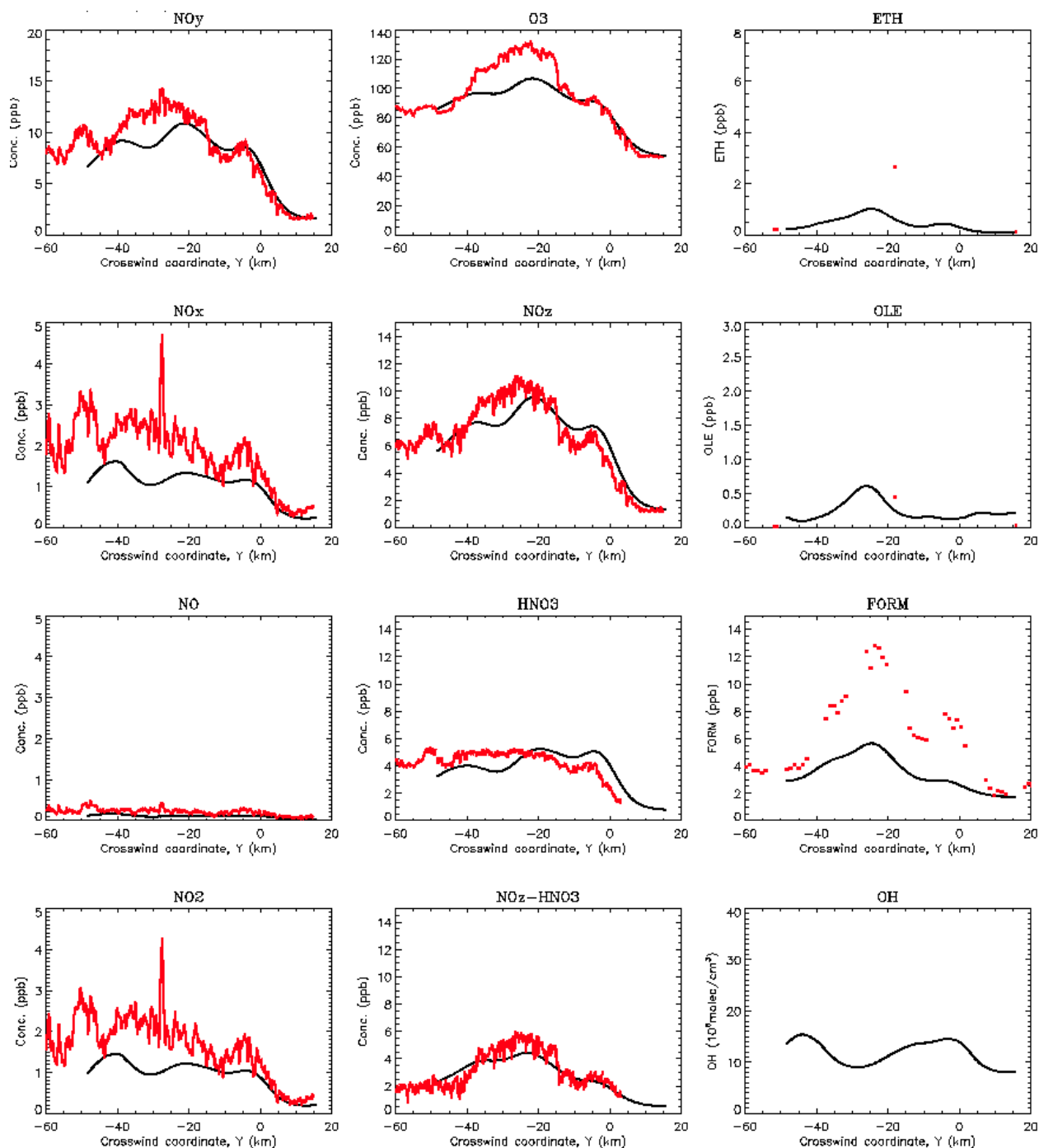**Model-data comaparison for Traverse T5, based on inferred emission rates of NOx, ETH and OLE**
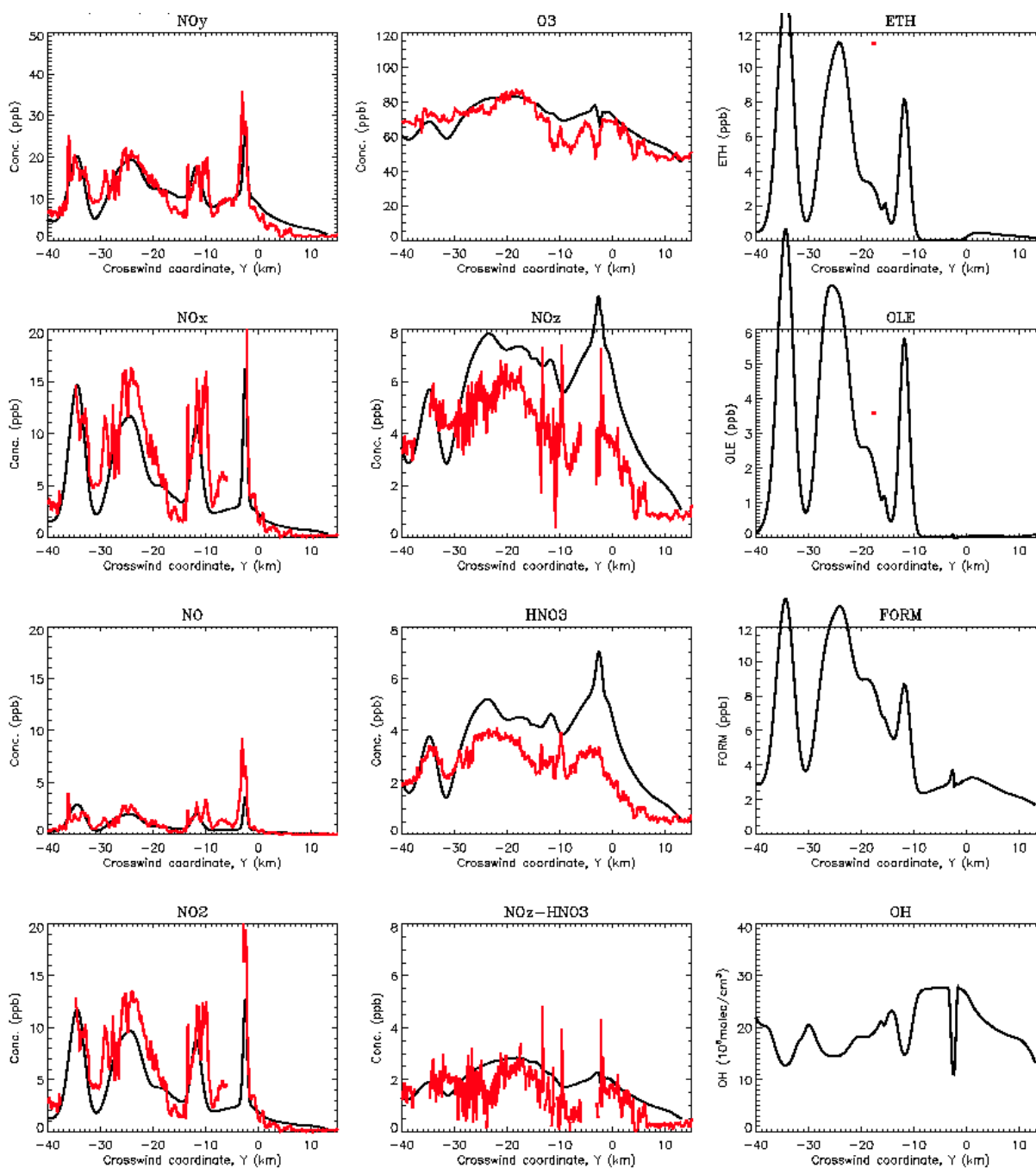
Figure 28. Comparison of measured (in red) and simulated (black) concentration profiles of primary and secondary species for traverse T5 (the first traverse, about 10 km, downwind of the ship channel complex). The simulation is based on inferred NOx and VOC emission rates as given in Table 1.

Model-data comaparison for Traverse T6, based on emission rates of NOx, ETH and OLE as in the EI
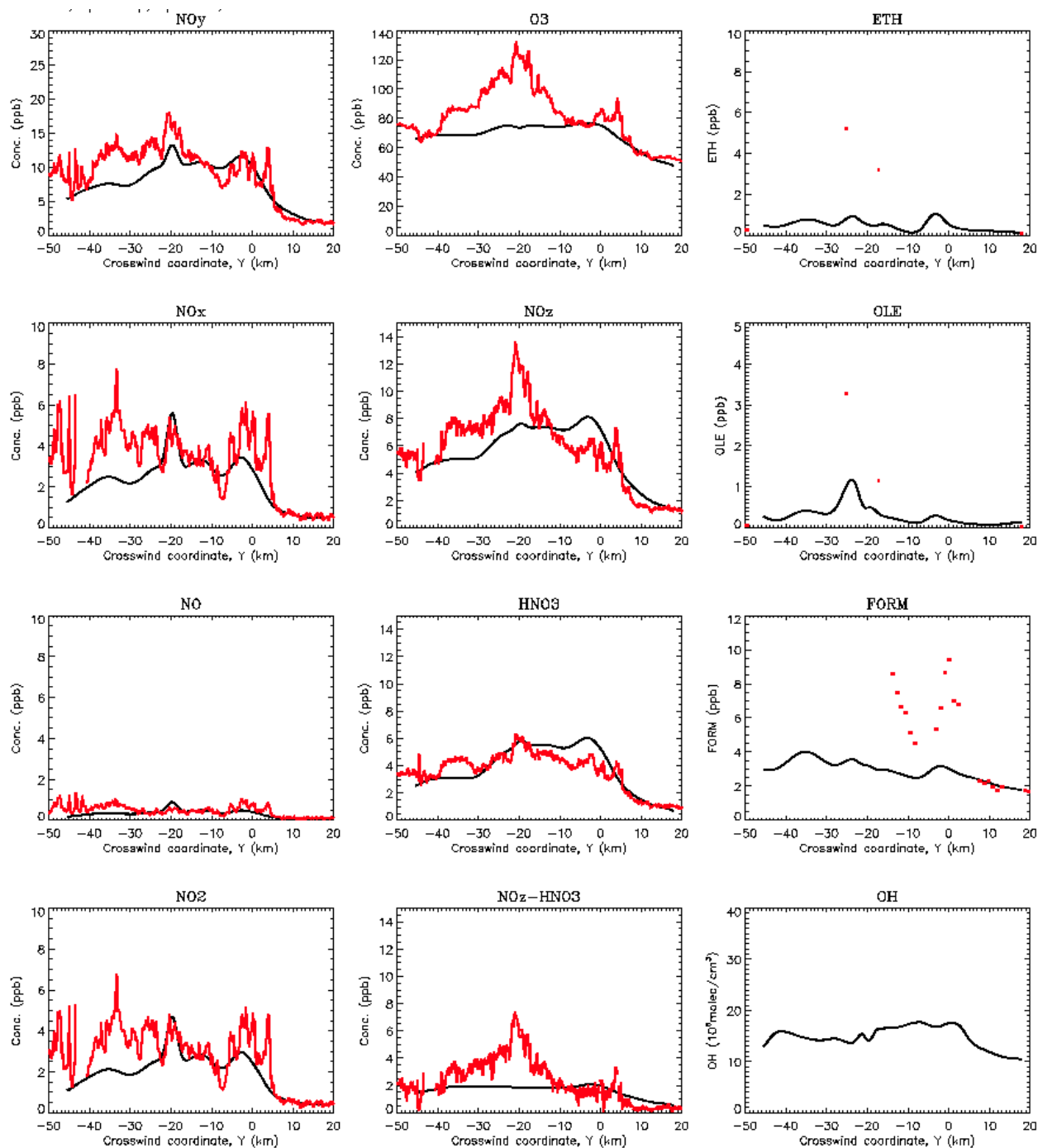
Figure 29. Comparison of measured (in red) and simulated (black) concentration profiles of primary and secondary species for traverse T6 (the second traverse, about 25 km, downwind of the ship channel complex). The simulation is based on NOx and VOC emission rates as in the emissions inventory (EI).

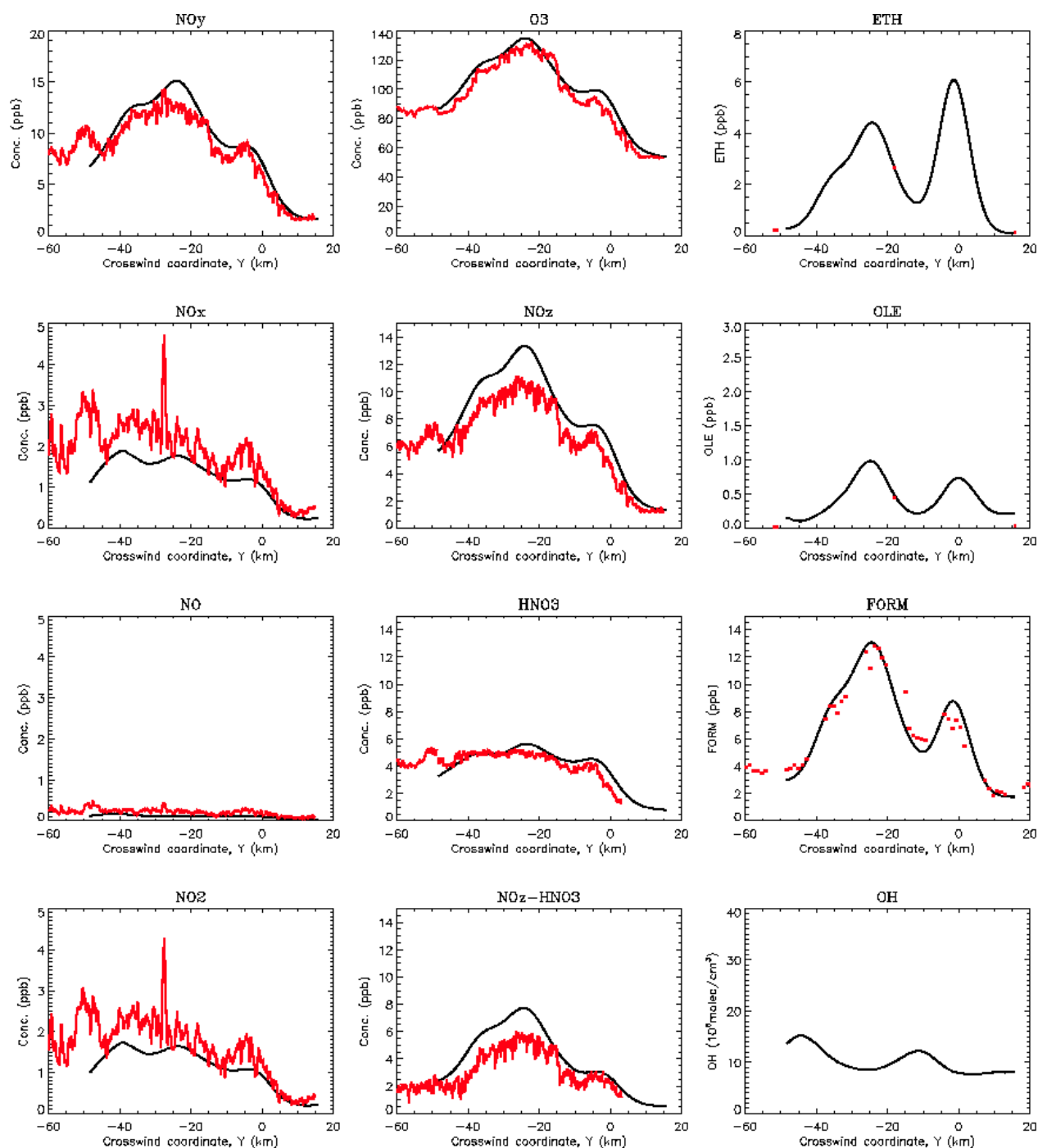**Model-data comaparison for Traverse T6, based on inferred emission rates of NOx, ETH and OLE**

Figure 30. Comparison of measured (in red) and simulated (black) concentration profiles of primary and secondary species for traverse T6 (the first traverse, about 25 km, downwind of the ship channel complex). The simulation is based on inferred NOx and VOC emission rates as given in Table 1.

Model-data comaparison for Traverse T7, based on emission rates of NOx, ETH and OLE as in the EI
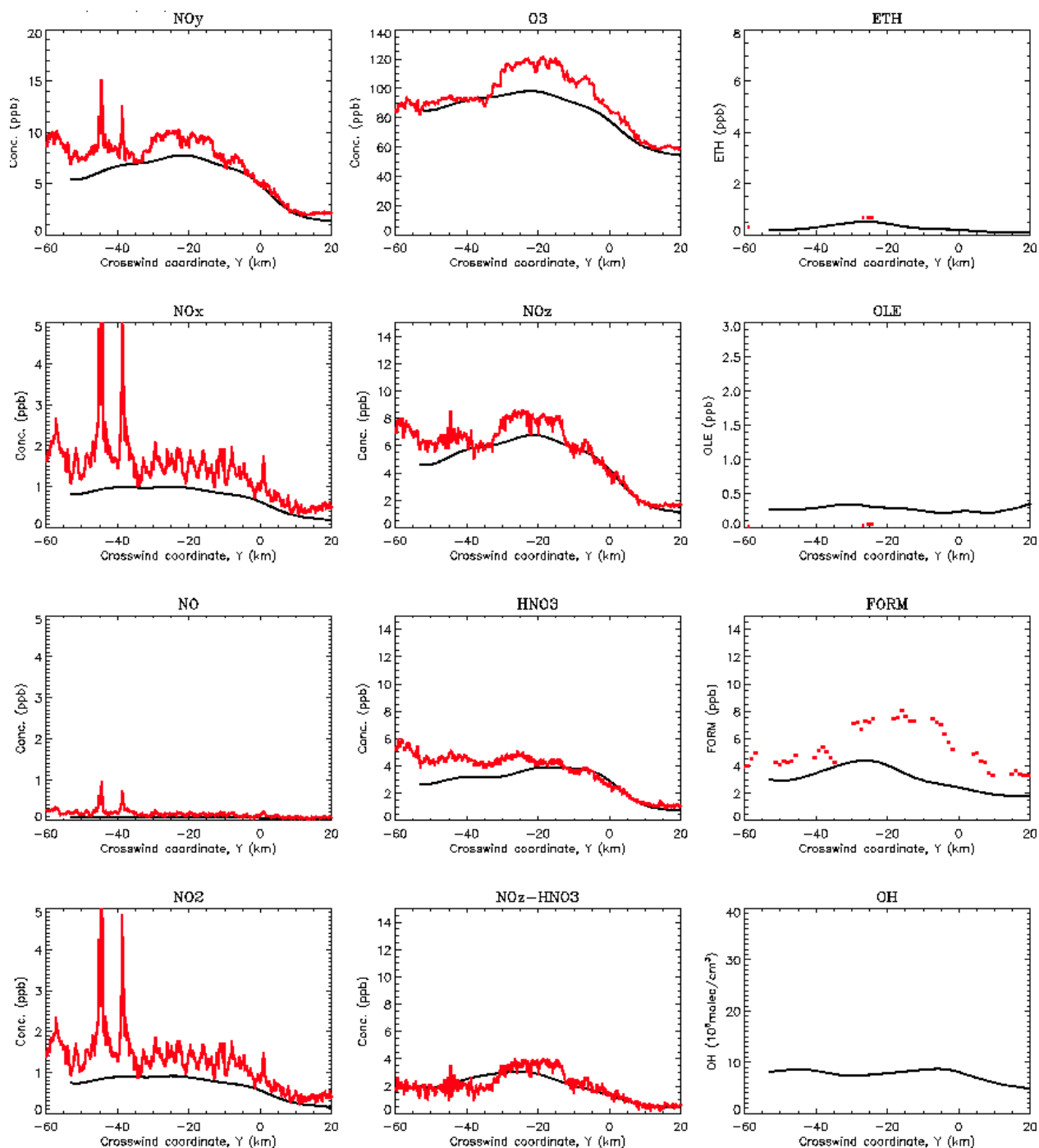

Figure 31. Comparison of measured (in red) and simulated (black) concentration profiles of primary and secondary species for traverse T7 (the third traverse, about 50 km, downwind of the ship channel complex). The simulation is based on NOx and VOC emission rates as in the emissions inventory (EI).

Model-data comaparison for Traverse T7, based on inferred emission rates of NOx, ETH and OLE
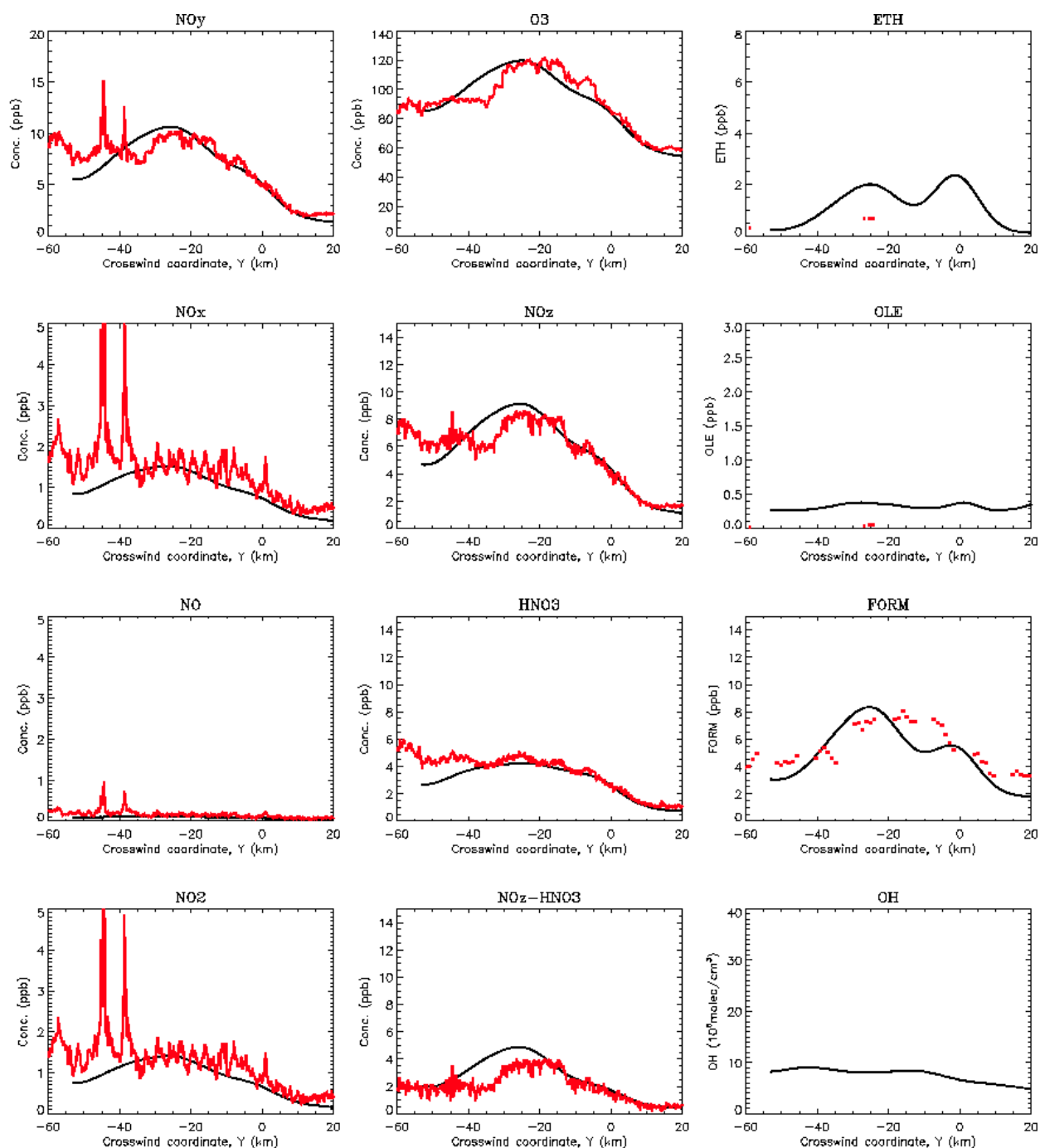

Figure 32. Comparison of measured (in red) and simulated (black) concentration profiles of primary and secondary species for traverse T7 (the third traverse, about 50 km, downwind of the ship channel complex). The simulation is based on inferred NOx and VOC emission rates as given in Table 1.

Model-data comaparison for Traverse T8, based on emission rates of NOx, ETH and OLE as in the EI

Figure 33. Comparison of measured (in red) and simulated (black) concentration profiles of primary and secondary species for traverse T8 (the fourth traverse, about 75 km, downwind of the ship channel complex). The simulation is based on NOx and VOC emission rates as in the emissions inventory (EI).

Model-data comaparison for Traverse T8, based on inferred emission rates of NOx, ETH and OLE

Figure 34. Comparison of measured (in red) and simulated (black) concentration profiles of primary and secondary species for traverse T8 (the fourth traverse, about 75 km, downwind of the ship channel complex). The simulation is based on inferred NOx and VOC emission rates as given in Table 1.